Modeling of plasma transport and negative ion extraction in a magnetized radio-frequency plasma source

G. Fubiani, Laurent Garrigues, G J M Hagelaar, Nicolas Kohen, Jean-Pierre Boeuf

Modeling of plasma transport and negative ion extraction in a magnetized radio-frequency plasma source

2017 New J. Phys. 19 015002

(http://iopscience.iop.org/1367-2630/19/1/015002)

New Journal of Physics
The open access journal at the forefront of physics

Deutsche Physikalische Gesellschaft DPG
IOP Institute of Physics

Published in partnership with: Deutsche Physikalische Gesellschaft and the Institute of Physics

OPEN ACCESS

RECEIVED
8 September 2016

REVISED
24 November 2016

ACCEPTED FOR PUBLICATION
29 November 2016

PUBLISHED
6 January 2017

PAPER

Modeling of plasma transport and negative ion extraction in a magnetized radio-frequency plasma source

G Fubiani, L Garrigues, G Hagelaar, N Kohen and J P Boeuf

LAPLACE, Université de Toulouse, CNRS, INPT, UPS, France

E-mail: gwenael.fubiani@laplace.univ-tlse.fr

Keywords: modeling, negative ions, particle in cell, plasma, ITER, ion source

Abstract

Negative ion sources for fusion are high densities plasma sources in large discharge volumes. There are many challenges in the modeling of these sources, due to numerical constraints associated with the high plasma density, to the coupling between plasma and neutral transport and chemistry, the presence of a magnetic filter, and the extraction of negative ions. In this paper we present recent results concerning these different aspects. Emphasis is put on the modeling approach and on the methods and approximations. The models are not fully predictive and not complete as would be engineering codes but they are used to identify the basic principles and to better understand the physics of the negative ion sources.

1. Introduction

Negative ion sources are used in a variety of research fields and applications [1] such as in tandem type electrostatic accelerators, cyclotrons, storage rings in synchrotrons, nuclear and particle physics (for instance to produce neutrons in the Spallation Neutron Source [2]) and in magnetic fusion devices (generation of high power neutral beams [3]). High brightness negative ion sources (i.e., which produces large negative ion currents) use cesium vapor to significantly enhance the production of negative ions on the source cathode surface. Cesium lowers the work function of the metal and hence facilitates the transfer of an electron from the metal surface to a neutral hydrogen atom by a tunneling process. The main types of devices that use cesium are magnetrons, Penning and multi-cusps ion sources. The former have applications in accelerators and the latter are often large volume ion sources like those developed for fusion applications. The plasma in large volume devices can be generated by hot cathodes (heated filaments) or radio-frequency (RF) antennas (inductively coupled-plasma, ICP discharges) standing either inside or outside the discharge [1]. Ion sources for fusion are tandem type devices with a so-called expansion chamber juxtaposed next to the discharge region. The expansion chamber is often magnetized with magnetic field lines perpendicular to the electron flux exiting the discharge. The magnetic field strength is typically of the order of ~100 G and is generated either by permanent magnets placed along the lateral walls of the ion source or via a large current flowing through the plasma electrode (which is also called 'plasma grid'). The plasma grid (PG) separates the ion source plasma from the accelerator region, where the extracted negative ions are accelerated to high energies. The axial electron mobility is strongly reduced by the magnetic field inside the expansion chamber and the electron temperature is hence significantly reduced as electrons loose a large amount of energy through collisions. In ion sources for fusion, the background gas pressure (either hydrogen or deuterium type) is ~0.3 Pa and the electron temperature is of the order of 10 eV in the discharge region. The magnetic filter reduces the electron temperature down to the eV level in the extraction region, close to the PG. The role of the magnetic filter field in the expansion chamber is threefold: (i) a large versus low electron temperature between the discharge and the extraction region allows the production of negative ions through the dissociative impact between an electron and an hydrogen (or deuterium) molecule $H_2(\nu \geqslant 4)$, where ν is the vibrational level. The vibrational excitation of the hydrogen molecule is maximized at high electron temperatures (typically $T_e \sim 10$ eV) while the cross-section for the dissociative attachment of H_2 and hence the production of a negative ion is the largest for $T_e \sim 1$ eV. (ii) A low electron temperature in the

vicinity of the PG significantly increases the survival rate of the negative ions and (iii) the magnetic filter more or less lowers the electron flux onto the PG but this is not sufficient and a suppression magnetic field is used to limit the co-extracted electron current. Co-extracted electrons have a damaging effect inside the electrostatic accelerator [4]. The electron beam is unfocused and induces a large parasitic power deposition on the accelerator parts. Note that in fusion-type, high power, large volume and low pressure ion sources, negatives ions produced via dissociative attachment of the background gas molecules (so called 'volume processes') range between 10%–20% of the total amount of extracted negative ion current [5, 6], the remaining part corresponds to ions generated on the cesiated PG surface through neutral atom and positive ion impacts. In magnetic fusion applications, negative ion sources are a subset of a neutral beam injector (NBI) producing high power neutral beams which are injected into the Tokamak plasma. Neutrals are insensitive to magnetic fields and can hence penetrate into the hot plasma core. The neutral beam provides power to the plasma, current (which is necessary to sustain the poloidal field) and are helpful to minimize the buildup of some type of instabilities. In the future International Thermonuclear Experimental Reactor (ITER), NBIs are designed to inject 33 MW of power (split over two beam lines) with an energy of 1 MeV into the Tokamak plasma [7]. The ITER project is the first fusion device which will mainly be heated by alpha particles (H_e^{2+}). The plasma will consist of Deuterium and Tritium ions providing 500 MW of fusion power. 50 MW of additional external power will be necessary in order to heat and control the plasma during the operating phase while the alpha particles will re-inject 100 MW of power to the fusion plasma (the total heating power is 150 MW). The remaining 400 MW is carried by the neutrons toward the wall of the Tokamak [8]. The external heating system for ITER also includes 20 MW of electron cyclotron heating at 170 GHz and 20 MW of ion cyclotron heating in the 35–65 MHz frequency range [9]. Total power is consequently 73 MW (including neutral beams), slightly above the required 50 MW for ITER.

In this paper we illustrate and analyze, on the basis of new results, the work performed in our group in the last ten years on the modeling and simulation of the negative ion source and negative ion extraction. The modeling of the negative ion source in all its complexity (power absorption, plasma chemistry, coupling with neutral transport and chemistry, transport across magnetic field, negative ion production and extraction) is a formidable task and we address the different questions separately with dedicated models using simplifying assumptions. In most cases the models are applied to the ITER prototype negative ion source BATMAN [5, 10–12] (BAvarian Test MAchine for Negative ions) developed at the Max-Planck-Institut für Plasmaphysik, Garching, Germany. The source is a tandem type device similar to the ITER configuration but with one ICP discharge (driver) and a smaller expansion chamber volume, accordingly. The driver dimensions are a cylinder of diameter 24.5 cm and length 16 cm [11, 13]. An external cylindrical antenna confers to the background gas (either molecular hydrogen or deuterium) about 100 kW of RF power, which generates a high density plasma of the order of $4 \times 10^{17} m^{-3}$ (averaged over the whole ion source volume). The expansion chamber, which is connected to the driver, has a larger volume and is magnetized; its size is approximately 57.9 cm in height, width of 30.9 and 24.4 cm in depth.

Most results presented and discussed in this paper have been obtained with particle-in-cell Monte Carlo collisions (PIC-MCC) methods. In section 2 we describe in details the method and discuss different points such as (1) parallelization, (2) use of scaling to make the simulations more tractable, (3) 3D versus 2D and 2.5D calculations, (4) a method for injecting power into the plasma (electron heating), (5) implementation of collisions (including physical-chemistry) and lastly (6) the modeling of the production of negative ions on the PG surface.

The negative ion source is a high density plasma in a large volume, i.e. the Debye length is much smaller than the dimensions of the source. The strong constraints on the grid spacing and time steps of a PIC-MCC simulation make it difficult to deal with the real values of the plasma density or dimensions. In several recent publications we have been using scaling of the plasma density (or, equivalently, of the vacuum permittivity) to keep the computation time within reasonable limits. Section 3 is devoted to the study of the effect of density scaling on the simulation results in a simplified problem of plasma transport across a magnetic filter where the Hall effect contributes to the cross-field transport and leads to plasma asymmetry (as in the ITER negative ion source).

We have previously published the results of a fluid model of the negative ion source where the plasma properties were analyzed as a function of power and pressure [14, 15]. The plasma fluid model was coupled to a fluid description of the neutral transport and chemistry. Interesting outcomes of the simulation were the strong neutral depletion due to gas heating and ionization, and the high temperature of hydrogen atoms with respect to molecules. The Knudsen number can be close to one in the negative ion source and this may have consequences on the velocity distribution functions of neutral particles. In section 4 we look at the possible effects of the low gas density on neutral transport and on the velocity distribution of hydrogen atoms and molecules. The particle transport in this section is described by a direct-simulation-Monte-Carlo (DSMC) model.

In section 5, we provide a detailed description of the plasma transport across the magnetic filter field inside the expansion chamber of the ion source (potential profiles, electron density and temperature). We discuss the

incidence of the Hall effect on the plasma dynamics (induction of a transverse asymmetry), the kinetics of negative ions and the role of positive ions in the production of negative ions on the cesiated surface of the PG. Section 6 compares the model predictions with experimental measurements. We show that the plasma asymmetry (and hence the incidence of the Hall effect) is observed in both cases. Section 7 analyses the numerical issues associated with the modeling of negative ion extraction from the PG surface. The simulation geometry is restricted to a zoom around a single aperture. PIC simulations are difficult to use with the real values of the plasma density. We present calculations obtained for plasma densities lower than in a real negative ion source and discuss the possible scaling laws that can be use to extrapolate the results to more realistic conditions.

2. Numerical model

2.1. PIC simulations

The principles of the PIC-MCCs method are described in textbooks [16, 17] and in various publications. In this section we discuss some specific issues associated with the simulation of ITER-type negative ion sources, i.e. (1) need to use parallel computing, (2) difficulty to simulate the high plasma density conditions of these sources (and consequences of performing density scaling), (3) 2D versus 2.5D and 3D calculations (4) implementation of a simplified model for the external power absorption inside the ICP discharge, (5) hydrogen plasma chemistry and (6) on the method to model the generation of negative ions onto the cesiated PG surface.

2.1.1. General features and parallelization of PIC-MCC simulation

We have developed and used 2D and 3D parallel Cartesian electrostatic explicit PIC-MCC models [16, 17] to study the plasma of negative ion sources for fusion. Due to he strong constraints on the grid spacing and time step in the high density plasma of negative ion sources, the PIC method must be optimized and parallelized. In this section we recall the principles of PIC-MCC simulations and briefly describe the technique of parallelization that is used in our models and its performance in term of computer time as a function of number of computer cores (or threads).

In an explicit algorithm, the particle trajectories are calculated based on the fields evaluated at the previous time step. The (self) electric field is derived self-consistently from the densities estimated on the grid nodes of the simulation domain. The magnetic fields, filter and suppression fields (the latter is generated by permanent magnets embedded in the first grid of the accelerator), are prescribed in this work. The time step must be a fraction of the electron plasma period and the grid size close to the electron Debye length, accordingly (both are set by the lightest of the simulated particles). The parallelization is performed in an hybrid manner using OpenMP [18] and MPI libraries. We use a particle-decomposition scheme for the particle pusher where each core (thread) have access to the whole simulation domain (as opposed to a domain-decomposition approach). The number of particles per core is nearly identical. We further implemented a sorting algorithm [19] in order to limit the access to the computer memory (RAM) and boost the execution time, Δt_{push}, of the pusher subroutine. The latter includes electron heating (inside the ICP discharge), field interpolations, update of the velocities and positions together with the charge deposition on the grid nodes. Particles are sorted per grid cell. The field and density arrays are hence accessed sequentially. Δt_{push} is shown in figure 1 normalized to the number of particles in the simulation. The best performance is obtained by attaching a MPI thread per socket and a number of OpenMP thread identical to the number of cores per socket. For the simulations of figure 1, we set the number of OpenMP threads to 10. We sort particles every 10 time steps without any loss of performance. The calculation is performed with a 3D PIC-MCC model and the numerical resolution is either $96 \times 64 \times 128$ grid nodes or eight times larger with 80 particles-per-cell (ppc). The time gained in the pusher with the particle sorting is a factor ~4. The sorting algorithm remains efficient as long as there is on average at least one particle per cell per thread. Beyond this limit Δt_{push} converges toward the value without sorting as shown in figure 1. We define the efficiency of the pusher without sorting as,

$$\beta = \frac{\Delta t^{(1)}_{\mathrm{push}}}{\Delta t_{\mathrm{push}} N_{\mathrm{core}}}, \tag{1}$$

where N_{core} is the number of cores (threads) and $\Delta t^{(1)}_{\mathrm{push}}$ the execution time of the pusher for $N_{\mathrm{core}} = 1$. β should be equal to 1 for a perfect parallelization of the pusher. We find $\beta \simeq 78\%$ for 20 cores, 70% for 320 cores and lastly, dropping to ~60% for 640 cores (i.e., about 23% loss in efficiency with respect to 20 cores).

Poisson's equation is solved iteratively on the grid nodes with a 3D multi-grid solver [20]. The latter is parallelized via a domain-decomposition approach. In multi-grid algorithms, a hierarchy of discretizations (i.e., grids) is implemented. A relaxation method (so-called successive-over-relaxation, SOR, in our case) is applied successively on the different grid levels (from fine to coarse grid levels and vice versa). Multigrid algorithms hence accelerate the convergence of a basic iterative method because of the fast reduction of short-wavelength

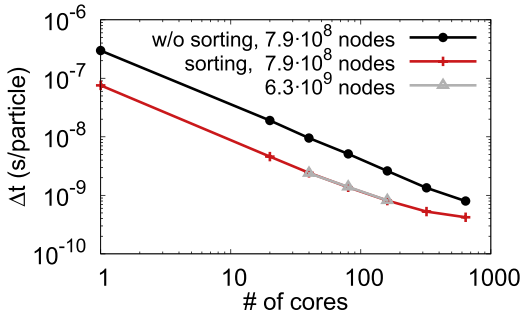

Figure 1. Execution time of the particle pusher (per time step) normalized to the number of macroparticles in the simulation versus the number of cores. The time is shown either with (red and gray lines) or without implementing a sorting algorithm (black-line). We use 80 particles-per-cell (ppc), a numerical resolution of 96 × 64 × 128 grid nodes (black and red lines) and 192 × 128 × 256 (gray line). The calculation is performed with a 3D PIC-MCC model on a 10 cores Intel Xeon processor E5-2680 v2 (25M cache, 2.80 GHz). There is 2 sockets per CPU, 20 cores in total.

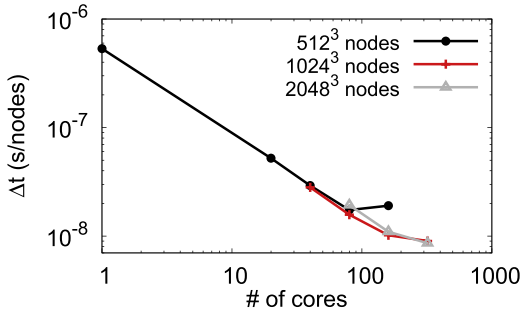

Figure 2. Execution time of the geometric multigrid Poisson solver (per time step) normalized to the number of grid nodes in the simulation versus the number of cores. the numerical resolution is 512^3 (black line), 1024^3 (red) and 2048^3 (gray) grid nodes, respectively. The calculation is performed on a 10 cores Intel Xeon processor E5-2680 v2 (25M cache, 2.80 GHz). We set the number of OpenMP threads to 10.

errors by cycling through the different sub-grid levels. Each sub-domain (i.e., a slice of the simulated geometry) is attached to a MPI thread while the do-loops are parallelized with OpenMP (SOR, restriction and prolongation subroutines [20]). Once there is less that one node per MPI thread in the direction where the physical domain is decomposed then the numerical grid is merged between all the MPI thread. The parallelization for the coarsest grids in consequently only achieved by the OpenMP threads. This is clearly a limiting factor and more work is needed to further improve the algorithm. As an example, using a mesh of 512^3 nodes, the speedup is about ∼30 for 80 cores ($\beta \simeq 40\%$). The execution time of the Poisson solver (normalized to the number of grid nodes) versus the number of cores in the simulation is shown in figure 2.

Lastly, for the numerical resolution which we typically implement to characterize the plasma properties of the ITER-prototype ion source at BATMAN, that is, 192 × 128 × 256 grid nodes with 20 ppc, the fraction of the execution time per subroutine averaged over one time step is, ∼55% for the particle pusher, ∼8% for the Poisson solver, ∼16% for Monte-Carlo (MC) collisions, ∼4% for the sorting. The remaining time concerns both the evaluation of the electric field and the calculation of the total charge density on the grid nodes (which involve some communication between MPI threads).

2.1.2. Scaling of PIC-MCC simulations

The high plasma density and large volume of negative ion sources make it practically impossible to perform multi-dimensional PIC-MCC simulations for real conditions. The ratio of discharge dimension to Debye length is on the order of 10^4 (tens of centimeters versus tens of micrometers) so a simple 2D PIC-MCC simulation in real conditions would involve 10^8 grid points and more than 10^9 super-particles. This is clearly prohibitive for parametric studies with 2D simulations and impossible for 3D. The 3D simulation of negative ion extraction is also difficult although the plasma density there is smaller than in the driver and one generally consider a small simulation domain around a grid aperture.

To overcome this problem, one solution is to perform some 'scaling' i.e. to run the simulations for more tractable conditions (e.g. smaller plasma densities or smaller dimensions) and extrapolate the results to the real conditions by using some scaling laws [21–24]. The simplest scaling is the scaling on plasma density. The

Boltzmann equation for electrons or ions is linear in the density of charged particles if the collision term is linear (i.e. when only charged particle collisions with neutrals are considered, with a given, constant velocity distribution function of neutral species), i.e. the equation is invariant if the distribution function (hence the charged particle density) f is divided by a constant α:

$$\frac{\partial \alpha^{-1} f}{\partial t} + \mathbf{v}.\frac{\partial \alpha^{-1} f}{\partial \mathbf{r}} + \mathbf{a}.\frac{\partial \alpha^{-1} f}{\partial \mathbf{v}} = I[\alpha^{-1} f], \tag{2}$$

where $\mathbf{a}$ is the acceleration of the charged particles due to the Lorentz force:

$$\mathbf{a} = \frac{q}{m}(\mathbf{E} + \mathbf{v} \times \mathbf{B}), \tag{3}$$

and I is the collision operator.

In a quasineutral plasma, the electric field is deduced from current continuity and is invariant when the plasma density n is divided by a constant α. This can be easily seen on the electron and ion momentum equations (from which the total current density can be deduced). A simplified form of the electron current density is:

$$en_e\mathbf{E} - \mathbf{J}_e \times \mathbf{B} = -\nabla P_e + m\nu_{en}\mathbf{J}_e, \tag{4}$$

where $\mathbf{J}_e$ is the electron current density, P_e the electron pressure and ν_{en} the electron-neutral collision frequency. In this equation, the electric field is invariant when the electron density is multiplied by a given factor. A similar argument can be made for ions.

Therefore we can conclude that the properties of a quasineutral plasma are not changed when the plasma density is scaled by a constant factor (for linear collision terms) and a PIC-MCC simulation of a quasineutral plasma can be performed with scaled densities. In a real problem the plasma is bounded which implies the presence of non-neutral Debye sheaths next to the walls. The sheath properties are clearly not invariant with a scaling of the plasma density (the sheath length is generally proportional to the Debye length), but the sheath voltage and hence the plasma potential do not depend on plasma density (the plasma potential depends only of the electron temperature and electron to ion mass ratio). Therefore, when a PIC-MCC simulation is performed with scaled densities (i.e. plasma density smaller that the real density) only the wall sheath thickness is modified. If the sheath thickness is still much smaller than the discharge dimensions the scaled simulation gives an accurate description of the real problem. However, care must be taken in the following situations:

- Since the sheath is larger for lower plasma densities it may become more collisional. The charged particle fluxes to the walls may be modified if the scaling is too important (ionization can also take place and be enhanced by secondary emission if present).
- In a magnetized plasma, the ratio of the charged particle gyroradius to the sheath length is also modified by the density scaling. This may also impact the charged particle transport and charged particle fluxes to the walls.
- The properties of the ion beam extracted from the plasma source are modified by the plasma density for a given extraction voltage (Child Langmuir law in the case of a collisionless sheath) and therefore the applied voltage should be scaled accordingly. This is clearly an important issue when scaling is used in a model of negative ion extraction (see section 7.5).
- In the presence of instabilities or turbulence associated with space charge separation (e.g. in a magnetized plasma) the density scaling no longer works. The instabilities and associated anomalous transport across the magnetic field do not scale linearly with the plasma density and density scaling cannot be used.

If Coulomb collisions (or other nonlinear collisions such as electron–ion recombination) are important in the real conditions, the collision module of the scaled PIC-MCC simulation can easily be modified to take into account the real collision frequencies (by using the real value of the target particle densities instead of the scaled value).

Note that in some published papers the scaling used is presented as a scaling of the vacuum permittivity instead of a scaling of the density [21–23]. It is easy to see (in Poisson's equation) that dividing the plasma density by a factor α is exactly equivalent to multiplying the vacuum permittivity by the same factor. In that case no scaling needs to be done for Coulomb collisions since the plasma density in the simulation is the real one.

Finally some authors have been using scaling on the discharge dimensions instead of a density scaling (see, eg, [25, 26]). In a *quasineutral plasma*, the system formed by the Boltzmann equations coupled with the generalized Ohm's law is invariant when the dimensions are reduced by a factor β provided that the gas density (i.e. collision operator) and magnetic field are multiplied by β (the time scale is also divided by β). The Boltzmann equation in that case can be written as:

$$\frac{\partial f}{\partial t/\beta} + \mathbf{v}.\frac{\partial f}{\partial \mathbf{r}/\beta} + \mathbf{a}.\frac{\partial f}{\partial \mathbf{v}} = I[f]. \quad (5)$$

We see that this equation is invariant if the collision term is multiplied by β, i.e. if the gas density is multiplied by β (the collision term is proportional to the gas density in the absence of Coulomb collisions), and if the acceleration, $\mathbf{a} = \frac{q}{m}(\mathbf{E} + \mathbf{v} \times \mathbf{B})$ is multiplied by β. The electric field E being a potential gradient is automatically multiplied by β when the dimensions are reduced by the same factor, while the external magnetic field B must be multiplied by β.

The scaling, defined above, on density, permittivity and dimensions, are all equivalent since in these three cases, the ratios λ_c/L and ρ_L/L are the same as in the real problem while the ratio λ_D/L is larger than in the real problem by a factor $\alpha^{1/2}$ in the density scaling and by a factor β in the dimensions scaling. The density scaling and dimensions scaling are therefore strictly identical, for a quasineutral plasma, if $\beta = \alpha^{1/2}$. λ_c, ρ_L, λ_D, and L are respectively the charged particle mean free paths, Larmor radii, Debye lengths, and discharge dimensions.

2.1.3. 2D, 2.5D, and 3D simulations

3D PIC-MCC calculations are restricted to low plasma densities, typically $\sim 10^{13}$ m^{-3} on 40 cores with $192 \times 128 \times 256$ grid nodes (20 ppc) for the prototype source at BATMAN. The density is about 10^5 times lower than the real density (i.e. $\alpha = 10^5$, see previous sub-section). In 2D rectangular PIC simulations, on the other hand, one may simulate a significantly larger plasma density. The plasma in the direction perpendicular to the simulation domain is implicitly supposed to be uniform and infinite and no charged particle losses along this direction are taken into account. A solution that allows to implement approximately the charged particle losses in the direction perpendicular to a 2D simulation domain without performing a 3D calculation is the so-called 2.5D model [23, 24]. For magnetized plasmas, the particle transport is simulated in the plane perpendicular to **B** (i.e. where the magnetized drift motion takes place). We assume that the plasma is uniform along the un-simulated direction, perpendicular to the 2D simulation plane (i.e., parallel to the magnetic field lines), and we use the following considerations to estimates the charged particle losses:

- The ion dynamics in the direction perpendicular to the 2D simulation plane is not calculated but we estimate the ion losses from the Bohm fluxes to the walls. The loss frequency at a given location in the simulation plane is obtained from [27] $\nu_L = 2hu_B/L_y$, where $u_B = \sqrt{eT_e(x, z)/m_i}$ is the local Bohm velocity, L_y is the length of the ion source in the third dimension, $h = n_s/\langle n \rangle \simeq 0.5$, n_s is the local plasma density at the sheath edge, $\langle n \rangle$ the averaged density, T_e (m_i), the local electron temperature (ion mass), respectively.
- The electron and negative ion trajectories are followed in the third dimension assuming that the plasma potential is flat (i.e., no electric field). When a negatively charged particle reaches a wall, it is removed if its kinetic energy along the un-simulated dimension is greater than the difference between the plasma potential and the wall, i.e., $1/2\ m_i v_z^2 \geqslant \phi(x, z)$ for a grounded wall. m_i is the particle mass.

Macroparticles are created anywhere between $0 \leqslant y \leqslant L_y$ in the third dimension (via ionization processes). The 2.5D model estimates plasma characteristics which are averaged over L_y. Note that this model is restricted to simplified magnetic field maps, where the field lines are straight in the un-simulated direction. The comparison between 2D, 2.5D and 3D models has been extensively discussed in [23].

2.1.4. External RF power absorption and Maxwellian heating in the driver

The ITER-type tandem reactors have an ICP discharge which couples a high RF power (typically 100 kW at 1 MHz frequency) to a hydrogen or deuterium plasma. We do not simulate directly the interaction of the RF field with the plasma but assume instead, a given absorbed power. Every time step, macroparticles which are found inside the region of RF power deposition are heated according to some artificial heating collision frequency. Electrons, being the lightest particles, are assumed to absorb all of the external power. Redistribution of energy to the heavier ions and neutrals is done through collisions (both elastic and inelastic) and the ambipolar potential. Electrons undergoing a heating collision have their velocities replaced by a new set sampled from a Maxwellian distribution with a temperature calculated from the average specie energy (inside the power deposition region) added to the absorbed energy per colliding particles, i.e.,

$$\frac{3}{2}T_h = \langle E_k \rangle_h + \frac{P_{abs}}{eN_{eh}\nu_h}, \quad (6)$$

where T_h(eV) is the heating temperature in electron-Volts (eV), $\langle E_k \rangle_h$ is the average electron energy, P_{abs} (W) is the absorbed power, ν_h the heating frequency and N_{eh} the number of electrons, respectively. For a given time step, $N_{em}\nu_h\Delta t$ colliding macro-electrons are chosen randomly where N_{em} is the total number of macroparticles inside the heating region.

The simulated electron temperature profile is constant inside the discharge region. This is consistent with plasma conditions which are found in devices running at low pressure, low RF frequency (~1 MHz) where electrons have typically a large thermal velocity in the driver ($T_e \sim 10$ eV), and a low collision frequency (a mean-free-path of the order of the discharge radius). These non-local heating conditions allow electrons, which can move freely, to deposit energy over the whole driver volume. Kinetic effects such as collisionless heating (leading to a so-called anomalous skin depth) and a non-negligible ponderomotive force (due to the high power and the low frequency of the RF antenna) are also expected inside the ICP discharge. The electron distribution function is typically non-Maxwellian in these conditions. A complete self-consistent model of the energy coupling in the ICP would be required to obtain a better estimation of the electron distribution in the driver. A non-self-consistent but much simpler and useful approach would be to study the influence of a non-Maxwellian distribution on the plasma parameters by imposing in the driver electron distributions that are deduced from experiments.

2.1.5. Implementation of collisions in a particle model—MC and DSMC methods

In a PIC-MCC algorithm, the Boltzmann equation,

$$\frac{\partial f_i}{\partial t} + \mathbf{v}.\frac{\partial f_i}{\partial \mathbf{r}} + \mathbf{a}.\frac{\partial f_i}{\partial \mathbf{v}} = \left(\frac{\partial f_i}{\partial t}\right)_c, \tag{7}$$

is solved numerically in two steps [28, 29].

$$\left(\frac{\partial f_i}{\partial t}\right)_c = \sum_t \iint (f_i' f_t' - f_i f_t) v_r \sigma_t^T \, \mathrm{d}\Omega \mathrm{d}v_t, \tag{8}$$

is the collision operator, f_i (f_t) is the distribution function for the incident (target) specie, respectively, m_i the mass, F the force field, $v_r = |v_i - v_t|$ the relative velocity, σ_t^T (v_r) the total differential cross-section (summed over all the collision processes between the incident and the target particles) and, lastly, Ω the solid angle. Primes denote the distribution function after the collision. For small time steps, equation (7) may be rewritten as,

$$f_i(x, v, t + \Delta t) = (1 + \Delta tI)(1 + \Delta tD) f_i(x, v, t), \tag{9}$$

where $f_i(x, v, t)$ is known explicitly from the previous time step. This finite-difference analog of equation (7) is second order correct in Δt. The operators D and I are,

$$D(f_i) = -\mathbf{v}.\frac{\partial f_i}{\partial \mathbf{r}} - \mathbf{a}.\frac{\partial f_i}{\partial \mathbf{v}}, \tag{10}$$

and $I(f_i) = (\partial f_i/\partial t)_c$. Applying the operator $(1 - \Delta tD)$ on the distribution function f_i is equivalent to solving the Vlasov equation,

$$\frac{\partial f_i}{\partial t} + \mathbf{v}.\frac{\partial f_i}{\partial \mathbf{r}} + \mathbf{a}.\frac{\partial f_i}{\partial \mathbf{v}} = 0. \tag{11}$$

The PIC procedure [16, 17] is a characteristic solution of equation (11). Once the particle trajectories have been updated, then the second operator $(1 - \Delta tI)$ may be applied on the (updated) distribution function. A macroparticle is equivalent to a Dirac delta function in position-velocity space (Eulerian representation of a point particle) and hence a probability may be derived from equation (9) for each collision processes [28, 29]. The probability for an incident particle to undergo an elastic or inelastic collision with a target particle during a time step Δt is

$$(P_i)_{\max} = \Delta t \sum_{c=1}^{N_c} (n_c \sigma_c v_r)_{\max}, \tag{12}$$

with N_c corresponding to the total number of reactions for the incident specie, n_c the density of the target specie associated with a given collision index and $v_r = |v_i - v_c|$. $(\sigma_c v_r)_{\max}$ is artificially set to its maximum value and hence $(P_i)_{\max}$ is greater than the real probability and is constant over the entire simulation domain. There is consequently a probability,

$$(P_i)_{\text{null}} = 1 - \sum_{c=1}^{N_c} \frac{P_c}{(P_i)_{\max}}, \tag{13}$$

that a particle undergoes a fake collision (dubbed 'null' collision), which will be discarded. $P_c = n_c \sigma_c(v_r) v_r \Delta t$. The total number of incident particles which will hence collide during a time step Δt (including a 'null' collision) is,

$$N_{\max} = N_i (P_i)_{\max}, \tag{14}$$

where N_i is the number of incident macroparticles in the simulation. N_i must be replaced by $(N_i - 1)/2$ for collisions with another particle of the same specie [28]. $(P_i)_{\max}$ is equiprobable for any pairs of incident-target

Table 1. Electron collisions.

#	Reaction	Cross section reference
1	$e + H \rightarrow e + H$ (elastic)	[71–75]
2	$e + H \rightarrow e + H$ (inelastic, 4 proc.)	[32]
3	$e + H \rightarrow 2e + H^+$	[32]
4	$e + H_2 \rightarrow e + H_2$ (elastic)	[76]
5	$e + H_2 \rightarrow 2e + H_2^+$	[32]
6	$e + H_2 \rightarrow 2e + H^+ + H$ (2 proc.)	[32]
7	$e + H_2 \rightarrow e + H_2$ (inelastic, 16 proc.)	[32–38]
8	$e + H_2 \rightarrow e + 2H$ (3 proc.)	[32, 77]
9	$e + H_3^+ \rightarrow 3H$	[32]
10	$e + H_3^+ \rightarrow H + H_2$	[32]
11	$e + H_3^+ \rightarrow e + H^+ + 2H$	[32]
12	$e + H_3^+ \rightarrow e + H^+ + H_2$	[32]
13	$e + H_2^+ \rightarrow 2H$	[32]
14	$e + H_2^+ \rightarrow e + H^+ + H$ (2 proc.)	[32, 77]
15	$e + H_2^+ \rightarrow 2e + 2H^+$	[77]
16	$e + H^- \rightarrow 2e + H$	[32]
17	$e + H_2^* \rightarrow H^- + H$ (1% of H_2)	[77]
18	$e + H_2^+ \rightarrow e + H_2^+$	(Coulomb) [22]
19	$e + H^+ \rightarrow e + H^+$	(Coulomb) [22]
20	$e + H_3^+ \rightarrow e + H_3^+$	(Coulomb) [22]

particles and consequently the latter may be chosen randomly inside the simulation domain. In the model, one checks first if the incident macroparticle experienced a real collision,

$$r \leqslant 1 - (P_i)_{\text{null}}, \tag{15}$$

where r is a random number between 0 and 1. The probabilities P_c for each reactions (whose total number is N_c for a given incident specie) are ordered from the smallest to the largest and a reaction k occurred if,

$$r \leqslant \sum_{c=1}^{k} \frac{P_c}{(P_i)_{\max}}. \tag{16}$$

Once a collision type is selected then the macroparticles (both incident and target) are scattered away in the center-of-mass (CM) frame (see next section). In the model, neutrals are either considered as a non-moving background specie with a given density profile or are actually implemented as macroparticles and their trajectories integrated. In the case of the former, collisions between charged particles and neutrals are performed by the so-called MC method while for the latter, actual particle–particle collisions are evaluated using a DSMC algorithm [30]. Both are similar except that in the MC method, one artificially extract a neutral particle velocity from a Maxwellian distribution function. Collisions between charged particles are always performed by a DSMC algorithm in the model. Collisions (both elastic and inelastic), are implemented assuming that particles (incident, target or newly created) are scattered isotropically in the CM. Energy and momentum is conserved and we assume for simplicity that each byproduct partner after the collision have identical momentum in the CM frame. This implies that the lightest particles will equally share most of the available energy. For further details, please refer to [21].

2.1.6. Physical chemistry of charged particles

We describe below the most complete version of the plasma chemistry module embedded in our PIC-MCC model (we often use a simplified sub-set of this module, depending on the purpose of the model). In this model, the plasma consists of electrons, molecular hydrogen (background) gas H_2, hydrogen atoms H, molecular ions H_2^+ and H_3^+, protons and lastly negative ions H^-. Collisions between electrons, ions and neutrals are considered; the set of reactions is presented in tables 1 and 2 (66 collision processes in total) and is very similar to the one used by previous authors [15, 31]. Table 1 corresponds to the collision processes associated with electrons. Reactions #2, 6, 7, 8 and 14 combine multiple inelastic processes included in the model in order to correctly account for the electron energy loss. Reaction #2 regroups the excitation of the hydrogen atom from the ground state to the electronic level $n = 2$–5 [32]. Reaction #7 combines the ground state excitation of the hydrogen molecule $H_2(X^1\Sigma_g^+;\ \nu = 0)$ to the vibrational levels $\nu' = 1$–3 [32, 33], electronic levels (for all ν') $B^1\Sigma_u$, $B'^1\Sigma_u$, $B''^1\Sigma_u$,

Table 2. Heavy particle processes.

#	Reaction	Cross section reference
1	$H_3^+ + H_2 \rightarrow H_3^+ + H_2$ (elastic)	[78]
2	$H_3^+ + H \rightarrow H_3^+ + H$ (elastic)	
3	$H_2^+ + H_2 \rightarrow H_3^+ + H$	[43, 78]
4	$H_2^+ + H_2 \rightarrow H_2 + H_2^+$	[78]
5	$H_2^+ + H \rightarrow H_2^+ + H$ (elastic)	[79]
6	$H^+ + H \rightarrow H + H^+$	[80]
7	$H^+ + H \rightarrow H^+ + H$ (elastic)	[80]
8	$H^+ + H_2 \rightarrow H^+ + H_2$ (elastic)	[78]
9	$H^+ + H_2 \rightarrow H^+ + H_2$ (inelastic, 4 proc.)	[41–43, 78]
10	$H^- + H \rightarrow e + 2H$	[32]
11	$H^- + H \rightarrow e + H_2$	[32]
12	$H^- + H_2 \rightarrow H^- + H_2$ (elastic)	[43]
13	$H^- + H \rightarrow H^- + H$ (elastic)	[43]
14	$H^+ + H^- \rightarrow 2H$ (2 proc.)	[32]
15	$H^+ + H^- \rightarrow H_2^+ + e$	[32]
16	$H^- + H_2 \rightarrow H_2 + H + e$	[32]
17	$H^- + H \rightarrow H + H^-$	[81]
18	$H + H \rightarrow H + H$	[80]
19	$H + H_2 \rightarrow H + H_2$	[80]
20	$H_2 + H_2 \rightarrow H_2 + H_2$	[82]

Table 3. Surface processes.

#	Reaction	Probability	Accommodation coef. γ	Reference
1	$H^+ \rightarrow H_2$	0.4	1	[44]
2	$H^+ \rightarrow H$	0.6	0.5	[44]
3	$H_2^+ \rightarrow H_2$	0.2	1	[45]
4	$H_2^+ \rightarrow H$	0.8	0.5	[45, 50]
5	$H_3^+ \rightarrow H_2$	1/3	1	None
6	$H_3^+ \rightarrow H$	2/3	0.5	None
7	$H \rightarrow H_2$	0.4	1	[44]
8	$H \rightarrow H$	0.6	0.5	[44]
9	$H_2 \rightarrow H_2$	1	1	None
10	$H^- \rightarrow H$	1	1	None

$C^1\Pi_u$, $D^1\Pi_u$, $D'^1\Pi_u$, $a^3\Sigma_g^+$, $c^3\Pi_u$, $d^3\Pi_u$ [32], Rydberg states [34] and lastly rotational levels $J = 2$ [35, 36] and 3 [37, 38]. Reaction #17 models in a simple manner the generation of negative ions in the ion source volume, which are a byproduct of the dissociative impact between an electron and molecular hydrogen $H_2(\nu \geqslant 4)$ [32]. The concentration of excited species is not calculated self-consistently in the model. To estimate the volume production of negative ions, we assume that 1% of H_2 molecules are excited in vibrational levels with $\nu \geqslant 4$. This is in accordance with the H_2 vibrational distribution function calculated either with a 0D model [39] or a 3D particle tracking code [40]. Table 2 summarizes the collision processes of heavy ions with neutrals. Reaction #9 corresponds to the excitation of the hydrogen molecule from the ground state to vibrationally excited levels $\nu' = 1$–2 [41, 42] and to the rotational levels $J = 2$–3 [43]. To our knowledge there is no reliable data available for the elastic collision between H_3^+ and neutral atoms (reaction #2), we consequently use the same cross-section as in reaction #1.

2.1.7. Physical chemistry of neutrals

Cross-sections for collisions between neutrals inside the ion source volume, which are summarized in table 2 (reactions #18-20), as well as backscattering, dissociation or recombination probabilities against the ion source walls are required for the modeling of the neutral particle dynamics (and the associated neutral depletion). Table 3 shows the surface processes and corresponding coefficients. In a low-pressure plasma device such as the one used for fusion applications (ITER or DEMO for instance. DEMO is a concept for the next generation of Tokamaks), the plasma-wall processes have a strong impact on the source characteristics. Low-temperature backscattered molecular hydrogen is assumed to be in thermal equilibrium with the wall. An average

backscattered energy is considered for fast atoms and ions, i.e. a thermal accommodation coefficient $\gamma < 1$ ($\gamma = 1$ corresponds to the wall temperature). These estimates are based on Monte Carlo calculations from the code TRIM [44]. Average reflection probability is also taken from the same database. Furthermore, we assume that atoms which are not backscattered will recombine. The interaction of H_3^+ and H_2^+ ions with the walls and the corresponding coefficients are not well known. The coefficients used in the simulations are reported in table 3. For H_2^+ we use coefficients that are consistent with the measurements of [45]. For H_3^+ we assume guessed values (the H_3^+ flux to the walls is relatively small with respect to the H_2^+ and H^+, and the results are not very sensitive to these coefficients).

2.1.8. Negative ions

Negative ions are produced on the cesiated PG surface as a byproduct of the impact of hydrogen atoms and positive ions. Our PIC-MCC model has not been coupled to a neutral transport module so the negative ion flux emitted by the surface is not obtained self-consistently from a flux of neutral atoms deduced from the simulation. The magnitude of the negative ion current density due to the impact of H atoms on the cesiated PG is either derived from plasma parameters measured experimentally or from DSMC calculations. Assuming a Maxwellian velocity distribution of the hydrogen atoms, the flux of these atoms on the PG is:

$$\Gamma_{\mathrm{H}} = \frac{1}{4} n_{\mathrm{H}} \sqrt{\frac{8eT_{\mathrm{H}}}{\pi m_{\mathrm{H}}}}, \tag{17}$$

where n_{H} is the atomic hydrogen density, m_{H} the mass and e the electronic charge. The negative ion current is deduced from,

$$j_{\mathrm{H}^-} = eY(T_{\mathrm{H}})\Gamma_{\mathrm{H}}, \tag{18}$$

with $Y(T_{\mathrm{H}})$ the yield [46], which was not obtained in a plasma (the experiment produced hydrogen from thermal dissociation in a tungsten oven) and consequently remains approximate for the ITER-type ion sources. For typical BATMAN working conditions, we find $n_{\mathrm{H}} \simeq 10^{19}\mathrm{m}^{-3}$, $T_{\mathrm{H}} \sim 1$ eV which gives $j_{\mathrm{H}^-} \sim 600$ A m^{-2} [47–49]. Negative ions are generated on the PG assuming a Maxwellian flux distribution function with a temperature $T_{\mathrm{n}} = 1$eV in the model. Furthermore, the surface production of negative ions resulting from positive ion impacts is calculated self consistently. For each ion impinging the PG, the yield is evaluated assuming a molecular ion may be considered as an ensemble of protons sharing the incident ion kinetic energy (a H_3^+ ion for instance would be equivalent to three protons each with an energy $E_k(H^+) = E_k(H_3^+)/3$). Each of these 'protons' may produce a negative ion. The condition $r \leqslant Y$ must be fulfilled for the negative ion to be generated with r a random number between 0 and 1. The yield is taken from Seidl *et al* [46] for Mo/Cs surface with dynamic cesiation. The negative ions are scattered isotropically toward the ion source volume with a kinetic energy assumed to be $E_k(H^-) = E_k(H^+)/2$. There is experimental evidence that negative ions may capture a large amount of the incident positive ion energy [50]. In addition, for clean metallic surfaces (tungsten) the reflected atomic hydrogen particle energy is numerically evaluated to be around 65% of the impact energy at normal incidence and for $E_k = 1$ eV [51]. Lastly, it has been reported in the experiments that the extracted negative ion current increases only slightly with cesium when the PG is water-cooled [52] while a PG heated to a temperature of ~100°C–250°C induces a significant increase of the negative ion current, by a factor ~4–5 in the experimental conditions of [5, 52] (the other walls of the ion-source were water-cooled). In the model, we consequently assume that negative ions may only be produced on the cesiated PG surface.

2.2. Simulation domain

The simulation domain for the 3D PIC-MCC modeling of the BATMAN device is shown in figures 3(a) and (b). The magnetic filter field is generated in the model by permanent magnet bars which are located on the lateral side of the ion source walls close to the PG. The field is calculated by a third-party code [53]. In 2.5D, solely the XZ plane is considered (figure 3(b)) but with a higher numerical resolution (or similarly plasma density) than in 3D. We assumed $L_y = 32$ cm for both the driver and the expansion chamber and we implemented a Gaussian profile for the magnetic filter (i.e., mirror effects are neglected [23]),

$$B_y(x, z) = B_0 \exp\left[\frac{-(x - x_0)^2}{2L_m^2}\right], \tag{19}$$

with an amplitude B_0, width L_m and a maximum located at x_0. The magnetic field generated by the permanent magnets has a shape very similar to a Gaussian profile on the ion source axis [23], as shown in figure 4. Figure 3(c) shows the simulation domain for higher numerical resolution 2D and 3D PIC-MCC modeling of negative ion extraction from the PG surface. $\mathbf{B}_{\mathrm{D}}$ corresponds to the deflection magnetic field from permanent magnets embedded into the extraction grid (EG). A domain restricted to the vicinity of the PG allows the implementation of plasma densities closer to the real one. This will be discussed in section 7.

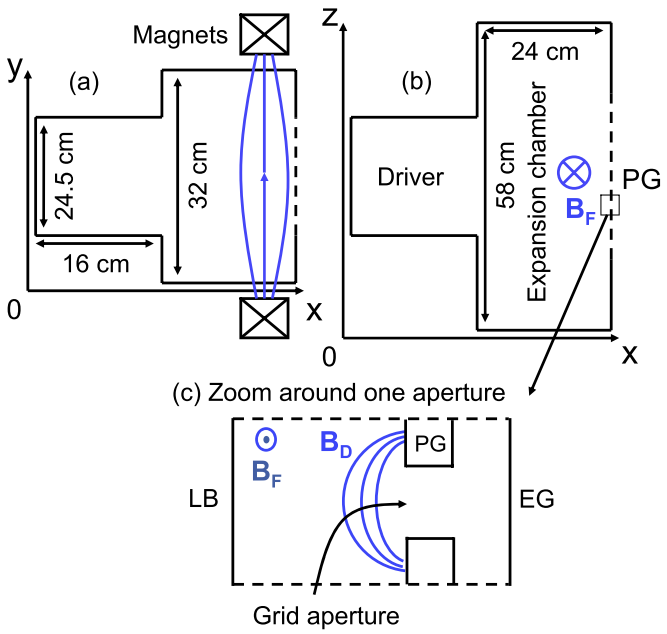

Figure 3. Schematic view of the BATMAN geometry. On the left side, the driver where the power from RF coils (unsimulated) is coupled to the plasma. The box on the rhs is the expansion chamber which is magnetized. The magnetic filter field $\mathbf{B}_F$ is generated by a set of permanent magnets located on the lateral walls of the chamber near the PG. Field lines are outlined in blue. The dashed line on the rhs of (a) and (b) correspond to the PG. The simulation domain for the modeling of negative ion extraction from the PG surface with a higher numerical resolution is displayed in (c). $\mathbf{B}_D$ is the magnetic field generated by permanent magnet bars embedded inside the extraction grid.

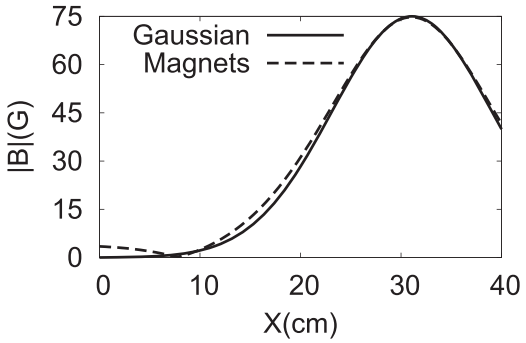

Figure 4. Magnetic filter field profile on the ion source axis ($Y = Z = 0$) for both the Gaussian case (solid line), equation (19) and the field generated by permanent magnets standing against the lateral side of the ion source walls (dashed lines). $B_0 = 75$ G, $L_m = 8$ cm and $x_0 = 31$ cm in this example (i.e., 9 cm from the PG).

3. Density scaling and Hall effect

As said above, the high plasma density and large volume of negative ion sources for fusion make it practically impossible to run full scale PIC simulations in 3D (and very difficult in 2D) and scaling the plasma density to lower values or the permittivity to higher values allow to perform computationally tractable simulations. As discussed in section 2.1.2 the scaling provides an approximate solution of the problem, the validity of the approximation depending for example on the size and role of the wall sheath in the considered problem.

In this section we provide a quantitative description of the effects of the density scaling in a simplified plasma source with magnetic filter. This example allows us to discuss both the influence of the density scaling on the results and the physics of the Hall effect induced by the presence of the magnetic filter and which contributes to non-collisional charged particle transport across the filter, and to the development of an asymmetry in the plasma properties.

3.1. Hall effect in a bounded plasma with a magnetic filter

It has been demonstrated in previous publications [14, 21, 22, 54] that the magnetized electron drift dynamics inside the magnetic filter induce a transverse plasma asymmetry in the expansion chamber. The effect of the magnetic field on electron transport can be analyzed from the fluid representation of the momentum equation (considering steady-state conditions),

$$\mathbf{\Gamma}_e = -\mu_e(\nabla P_e + n_e\mathbf{E} + \mathbf{\Gamma}_e \times \mathbf{B}), \tag{20}$$

where $\mu_e = |e|/m_e\nu_e$ is the electron mobility without magnetic field, e is the elementary charge, $P_e = n_e T_e$ is the electron pressure, n_e the electron density, T_e the temperature (in electron-Volts), $\mathbf{\Gamma}_e = n_e\mathbf{u}_e$ the electron flux and lastly, $\mathbf{B}$ the magnetic filter field. Equation (20) assumes that the electron distribution function is approximately a Maxwellian and neglects viscosity and inertia effects (the latter are of course taken into account in a PIC simulation). The electron flux diffusing from the driver toward the extraction region experiences a Lorentz force perpendicular to the direction of the flux and the magnetic field (same direction as the cross product $\mathbf{J}_e \times \mathbf{B}$, where $\mathbf{J}_e = -e\mathbf{\Gamma}_e$ is the electron current density). The force is directed toward the bottom surface of the ion source for the filter configuration schematically shown in figure 3(b). The presence of walls induces a charge separation (polarization) and the creation of an average electric field that opposes the effect of the Lorentz force, as in the Hall effect. This Hall electric field (which is consequently downward-directed), $\mathbf{E}_H$, generates in turn an $\mathbf{E}_H \times \mathbf{B}$ drift along the X-axis which significantly increases electron transport across the magnetic filter with respect to an ideal 1D filter without transverse walls [54, 55]. We therefore expect that the Hall effect will create a plasma asymmetry with an electric potential and a plasma density higher in the top of the chamber (large Z) than in the bottom (small Z). The electron flux in equation (20) may be expressed as follows [21],

$$\mathbf{\Gamma}_e = \frac{1}{1+h^2}[\mathbf{G} + \mathbf{h} \times \mathbf{G} + (\mathbf{h}\cdot\mathbf{G})\mathbf{h}], \tag{21}$$

with,

$$\mathbf{G} = -\mu_e(n_e\mathbf{E} + \nabla P_e), \tag{22}$$

where $h_B = \Omega_e/\nu_e = \mu_e B$ is the Hall parameter. Note that $\mathbf{\Gamma}_e = \mathbf{G}$ when $\mathbf{B} = 0$. In fusion-type negative ion sources $h \gg 1$ and in the plane perpendicular to the magnetic field lines ($\mathbf{h}\cdot\mathbf{G} = 0$), we have,

$$\mathbf{\Gamma}_e \simeq -\frac{\mathbf{G}\times\mathbf{B}}{\mu_e B^2}. \tag{23}$$

The electron motion is consequently dominated by the magnetic drift which is composed of a diamagnetic term $\nabla P_e \times \mathbf{B}$ (collective effects), and an $\mathbf{E} \times \mathbf{B}$ term [54, 56]. The electric field is a combination of the Hall and the ambipolar fields.

The Hall effect in low temperature plasmas and its impact on plasma asymmetry have been studied analytically in the simple conditions of a positive column [57, 58]. The situation is more complicated in the magnetic filter of the negative ion source because of the non-uniform magnetic field and of the presence of axial plasma density gradients. Furthermore, the general features of the Hall effect (i.e., production of a voltage difference across an electrical conductor, perpendicular to both the direction of the electric current in the conductor and the applied magnetic field) have been clearly observed in other magnetized plasma sources with particle transport properties comparable to those of the ITER prototype ion sources. Experimental measurements have been recently performed in a low power inductively coupled plasma with a magnetic filter and have shown the presence of a strong asymmetry in the collected current density [59]. Note finally that the Hall effect is not present in devices such as Hall thrusters where the electron drift perpendicular to the discharge current is closed and is not impeded by the presence of walls (closed-drift devices).

3.2. Transport across a filter in a simplified geometry and influence of density scaling

In order to illustrate the Hall effect in magnetized plasmas in a simplified manner, and, at the same time study the influence of density scaling on the results, we implemented a 2D simulation domain which is a square box of dimensions 20×20 cm^2. The model is a 2D PIC-MCC and there is no particle losses in the plane perpendicular to the simulation domain. We model the XZ plane and the magnetic filter field is along (OY) as in figure 3(b). The magnetic field profile is given by equation (19) with $B_0 = 20$ G, $L_m = 2$ cm and $x_0 = 10$ cm. We consider only electrons and H_2^+ ions as particle species composing the plasma and therefore we use a subset of the physical-chemistry described in tables 1 and 2. Instead of assuming that an external power is absorbed by the plasma, as described in section 2.1.4, we keep the plasma density constant by re-injecting an electron–ion pair each time a positive ion is lost on the external boundaries of the simulation domain. The latter are absorbing surfaces. The particle re-injection is set inside a magnetic field free region between $x = 1.5$ and 4.5 cm. Furthermore, the electron temperature is maintained constant in that area with $T_e = 10$ eV. The scope is to draw an electron current (flux from left to right) through the magnetic filter and evaluate the Hall effect. For that

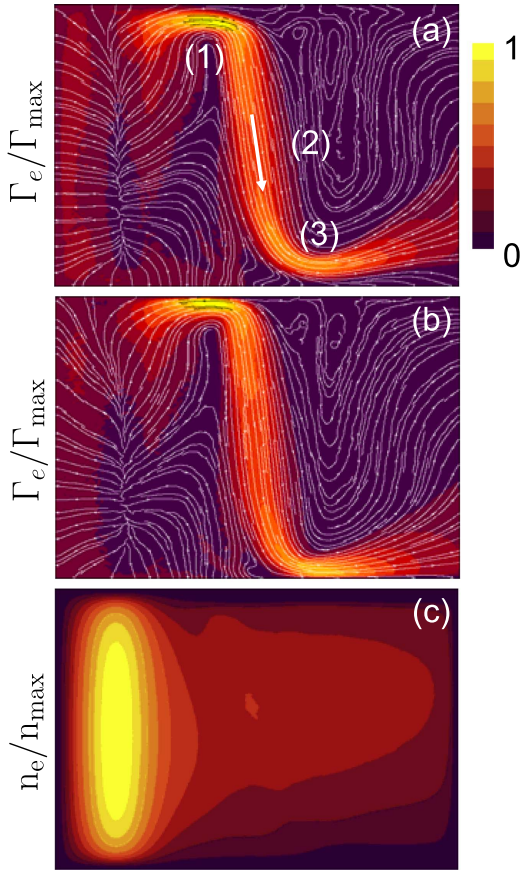

Figure 5. Electron flux profile in the *XZ* plane for an average plasma density of $\langle n_p \rangle = 10^{14}$ m^{-3} (with $\Gamma_{max} = 2.5 \times 10^{19}$ m^{-2} s^{-1}) in (a), and $\langle n_p \rangle = 6.4 \times 10^{15}$ m^{-3} ($\Gamma_{max} = 1.45 \times 10^{21}$ m^{-2} s^{-1}) in (b). The electron density is shown in (c). $n_{max} = 2.75 \times 10^{14}$ m^{-3}. The magnetic filter field is directed along (OY) with a Gaussian profile axially ($B_0 = 20$G, $L_m = 2$ cm and $x_0 = 10$ cm). The boundaries of the simulation domain are of Dirichlet type and grounded except the rhs surface which is biased, $V_{bias} = 20$ V. The numerical resolution is 256^2 grid nodes in (a) and 2048^2 nodes in (b) with 40 ppc. The model is a 2D PIC-MCC.

purpose we assume that there is no ionization processes and hence reaction #5 in table 1 is artificially replaced by an inelastic collision (excitation). The density profile of molecular hydrogen is constant with $n_{H_2} = 5 \times 10^{19}$ m^{-3} and we bias the rhs electrode positively with respect to the other surfaces, $V_{bias} = 20$ V. Figure 5 shows the electron flux profile in the *XZ* plane for two plasma densities, that is, $\langle n_p \rangle = 10^{14}$ m^{-3} in (a) and $\langle n_p \rangle = 6.4 \times 10^{15}$ m^{-3} in (b). The profiles are very similar except that the electron flux channels closer to the walls in the higher density case. This is due to the transverse shape of the plasma potential. The size of the Debye sheath is smaller and hence the pre-sheath extends closer to the boundaries. This also indicates that the electron motion across the magnetic filter field occurs mainly in the pre-sheath. This is confirmed by quasi-neutral fluid calculations. The maximum value of the Hall parameter is $h_{max} \simeq 40$ in the model and the electron flux is hence well described by equation (23). The electron flux is a combination of a diamagnetic drift, which is a consequence of the particle random motion (i.e., the velocity spread) expressed mathematically in the pressure term and an $\mathbf{E} \times \mathbf{B}$ drift. The two terms are often of opposite sign, i.e., cancelling each others. The electric field is itself a combination of the Hall (which is downward directed) and ambipolar fields as demonstrated in section 3. In the regions (1) and (2) highlighted in figure 5(a), we find $|\nabla P_e|/n_e > |\mathbf{E}|$ and the electron transport is driven by the diamagnetic drift while in (3), $|E_y| > |n_e^{-1} \partial P_e/\partial y|$, i.e., the drift is of $\mathbf{E} \times \mathbf{B}$ type, respectively. The electron current density profile depends on the shape and magnitude of the magnetic filter field but the general features described in this section are reproduced in any type of magnetized plasma sources where a current is drawn across the magnetic field (biasing the rhs electrode hence enhance the Hall effect). Figure 5 shows that the plasma density has a small influence on the plasma properties in the considered range (the ratio of the plasma density between the two simulations is equal to 64). Charged particle transport in the plasma occurs mainly inside the quasi-neutral region driven by the pressure gradient, the ambipolar and Hall electric fields, and the effect of the sheath on the electron current density distribution is negligible on the figure. The sheath should be about 8 times larger in the lower plasma density case of figure 5(a). Note that the presence of the magnetic filter can also induce plasma instabilities seeded by charge separation. This happens, in the simulations of the simplified problem considered here, when the length of the transverse direction is significantly increased. In that

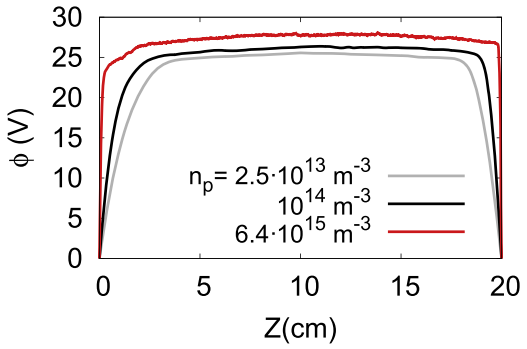

Figure 6. Transverse plasma potential profile (at $X \simeq 13.4$ cm) versus the average plasma density inside the simulation domain. The numerical resolution is 128^2 grid nodes for $\langle n_p \rangle = 2.5 \times 10^{13}$ m^{-3} up to 2048^2 nodes for $\langle n_p \rangle = 6.4 \times 10^{15}$ m^{-3}. 40 ppc was used in the model.

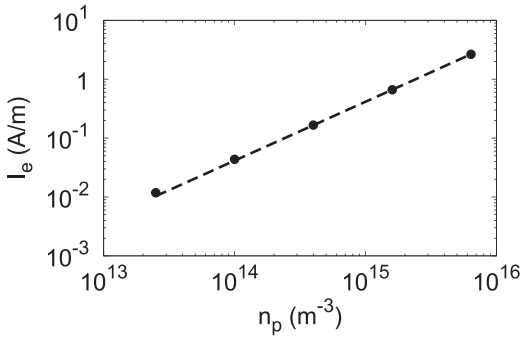

Figure 7. Electron current (black dots) collected on the biased electrode (rhs of the simulation domain) versus the plasma density. The dashed line corresponds to a straight line between the origin ($n_p = 0$) and the last data point.

case the Hall effect is no longer sufficient to ensure cross-field transport and instabilities develop, enhancing electron transport across the filter. The asymmetry of the plasma density resulting from the Hall effect can be seen in figure 5(c).

Figure 6 which shows the transverse plasma potential profile versus the average plasma density. The latter is increased from $\langle n_p \rangle = 2.5 \times 10^{13}$ m^{-3} up to $\langle n_p \rangle = 6.4 \times 10^{15}$ m^{-3}. The ratio of the densities between the two extreme cases is $\alpha = 256$. The variations between the potential profiles in figure 6 lie essentially on the size of the Debye sheath. The amplitude of the potential in the quasi-neutral region is similar within ~10%. The Hall electric field E_H is about 15 V m^{-1} (measured between the top and bottom plasma sheath edges). Figure 7 shows the electron current collected on the biased electrode (rhs of the simulation domain) versus the plasma density. The current increases linearly with the plasma density as expected.

One may qualitatively estimate the ratio of the simulation domain occupied by the plasma sheath by comparing the average electron Debye length $\bar{\lambda}_{De}$ with respect to a characteristic length defined as $L_s = \sqrt{V_s} = 20$ cm, where V_s is the ion source volume. We find $\bar{\lambda}_{De} \simeq 3.7$ mm for $\langle n_p \rangle = 2.5 \times 10^{13}$ m^{-3} and a sheath width of $L_{sh} \sim 4\bar{\lambda}_{De}$, giving a ratio of $2L_{sh}/L_s \sim 15\%$.

4. Neutral transport and plasma properties versus power and pressure

In a previous work we studied the properties of the plasma of the negative ion source versus power and pressure based, on a quasineutral fluid description of the plasma, coupled with a Navier–Stokes model of neutral transport [14, 15]. It was shown that the neutral density was strongly depleted due to gas heating and ionization and that the temperature of atomic hydrogen was much larger than that of molecular hydrogen. In this section we use the same plasma model but we couple it with a kinetic description of neutral transport based on a DSMC method. The objective is to estimate the consequences of the fact that the gas flow is rarefied (Knudsen number not small with respect to 1) on the model results and on the velocity distribution of hydrogen atoms and molecules.

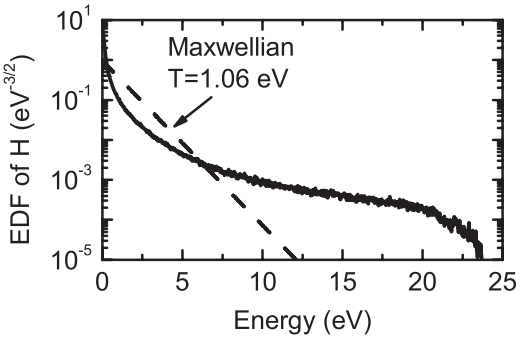

Figure 8. Energy distribution function for atomic hydrogen in the center of the negative ion source. We implemented a 60 kW absorbed power, 0.3 Pa background gas pressure and no magnetic filter field.

Table 4. Particle and power source (loss) terms for the production (destruction) of hydrogen atoms inside the ion source (60 kW absorbed power, 0.3 Pa, no magnetic filter field).

#	Reaction	Particles	Power
	Source terms		
1	$H_x^+ \rightarrow$ H (surface)	45.6%	77.2%
2	$e + H_2 \rightarrow e + 2H$	47.6%	19.6%
3	Other processes	6.8%	3.2%
	Loss terms		
4	$e + H \rightarrow 2e + H^+$	14.2%	2.4%
5	$H + H_2 \rightarrow H + H_2$	—	3.6%
6	$H \rightarrow$ H (surface)	—	40.4%
7	$H \rightarrow H_2$ (surface)	85.8%	53.6%

4.1. Modeling of the neutral transport and chemistry in the ITER prototype ion source

In the ITER prototype source BATMAN, the typically working conditions correspond to a low background gas pressure (molecular hydrogen or deuterium) of ~0.3 Pa, together with a high RF power (coupled to the plasma by an external antenna), ~100 kW. Such conditions depletes the neutrals in the experiments [47]. This effect was first described through modeling [15] and then confirmed by experiments [47]. We model neutral depletion by coupling a DSMC algorithm for the neutrals (both molecular and atomic hydrogen in our case) with the 2D implicit fluid model described in details in [14]. In this self-consistent model, the plasma parameters adjust so that charged particle and power balance are satisfied at steady state (e.g. volume ionization is compensated by surface losses). The geometric parameter involved in the charged particle and power balance is the chamber volume over surface ratio therefore the dimensions of the 2D geometry are rescaled accordingly in the model of BATMAN [23]. The dimensions of the ion source in the model is a driver of length 9 cm, height 8 cm and an expansion chamber of 16 × 16 cm^2. The flow rate for the molecular hydrogen gas injected into the ion source volume is adjusted, $Q_{H_2} \simeq 0.17$ Pa m^3 s^{-1}(i.e., 4.2 × 10^{19} H_2 s^{-1}), in order to conserve a residence time for the molecules similar to the experiments ($\tau \simeq 57$ ms in BATMAN).

Figure 8 shows the atomic hydrogen energy distribution function in the center of the negative ion source for a 60 kW absorbed power and 0.3 Pa background gas pressure. The distribution function is highly non-Maxwellian and its properties are mostly controlled by the production and collisions of H atoms against the walls of the ion source (the total mean-free-path is of the order of 1 m, i.e., significantly larger than the dimensions of the device). Reactions which either generate (so-called source term) or remove (loss term) hydrogen atoms from the ion source volume are summarized in table 4. Particle and power (gain or loss) are shown as a percentage of the total. H atoms are mostly created and heated by the wall recombination of protons and molecular ions on the ion source walls (reaction #1 with ≃45% of the particle production and ≃77% of the energy gain) and by the volume dissociation of H_2 (reaction #2). H_x^+ ions (where $x = 1$–3) are mainly generated inside the discharge and are accelerated by the plasma potential toward the walls of the ion source. The amplitude of the potential in the driver is about 50 V for 60 kW of RF power at 0.3 Pa in the experiments [11]

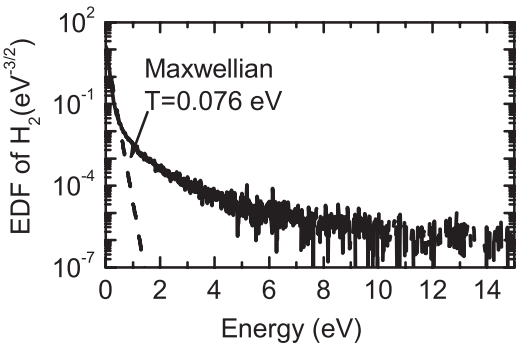

Figure 9. Energy distribution function for molecular hydrogen in the center of the negative ion source (60 kW absorbed power, 0.3 Pa, no magnetic filter field).

Table 5. Particle and power source (loss) terms for the production (destruction) of H_2.

#	Reaction	Particles	Power
	Source terms		
1	$H + H_2 \rightarrow H + H_2$	—	66%
2	$e + H_2 \rightarrow e + H_2$	—	13.7%
3	$H_x^+ \rightarrow H_2$ (surface)	17.3%	1.4%
4	$H \rightarrow H_2$ (surface)	82.7%	6.7%
5	Other processes	<0.1%	12.2%
	Loss terms		
6	$e + H_2 \rightarrow e + 2H$	45.9%	6.4%
7	$e + H_2 \rightarrow 2e + H_2^+$	46.5%	6.5%
8	$H_2 \rightarrow H_2$ (surface)	—	85.9%
9	Other processes	7.2%	1.2%

and hence H_x^+ ions impact the walls with a high energy. This explains the origin of the large energy tail in the distribution function of atomic hydrogen as shown in figure 8. Lastly, H atoms loose most of their energy through collisions with the source walls (~95%, reactions #6 and 7). The H and H_2 temperatures are strongly dependent on the assumptions that are made on the wall reactions (accommodation coefficients provided in table 3).

The energy distribution function for molecular hydrogen is shown in figure 9. H_2 molecules are created uniquely through the recombination of H_x^+ ions and H atoms on the walls. Molecular hydrogen is emitted from the surfaces as a Maxwellian flux at $T_w = 300$ K (where T_w is the temperature of the surface). The energy distribution function is well fitted by a Maxwellian (up to about $6T_{H_2}$). The mean-free-path is ~10 cm, i.e., smaller than the dimension of the ion source. The energy tail is induced by the collisions with the warm H atoms ($T_H \simeq 1$ eV for 60 kW and 0.3 Pa while $T_{H_2} \simeq 0.08$ eV). Molecular hydrogen is mainly heated through elastic collisions with atoms (~65% of power gain, reaction #1) and by electrons (reaction #2) as shown in table 5.

The calculations have been performed either with or without a magnetic filter field in the expansion chamber. The magnetized case corresponds to a maximum field amplitude of $B_{max} = 15$G close to the PG, which is lower than the field in the actual experiment (~75 G on axis) but nevertheless $h_B = \mu_e B \gg 1$ and the electrons are fully magnetized (a smaller magnetic field is used in the simulation because of numerical issues at the time with the fluid model for large magnetic fields). The indirect effect of the magnetic field on the neutral dynamics is that the depletion of H_2 occurs in the area where the electron density is highest (i.e. in the driver when the expansion chamber is magnetized) because molecular hydrogen is dissociated or ionized mainly by electrons (table 5). The density profile of hydrogen atoms is on the contrary quite insensitive to the magnetic field due to the fact that the volume losses (ionization) are significantly smaller than for H_2 (i.e., ~14% of the total losses, see table 4) and that the mean free path, ~1 m, greatly exceeds the ion source dimensions. The 2D density and temperature profiles for the H atoms are shown in figure 10. Figure 11 displays the electron density and temperature averaged over the negative ion source volume versus the absorbed RF power in the discharge and the background gas pressure. For a pressure of 0.75 Pa, the electron temperature is almost independent of the external power while the electron density increases quasi-linearly with power. This behavior may be

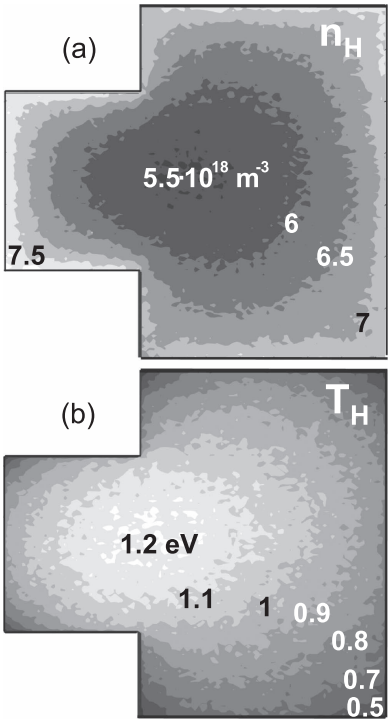

Figure 10. Atomic hydrogen density (a) and temperature (b) profiles. 2D DSMC calculation with $P_{abs} = 60$ kW, a background gas pressure of 0.3 Pa, $B_{max} = 15$ G and a PG bias voltage of 10 V.

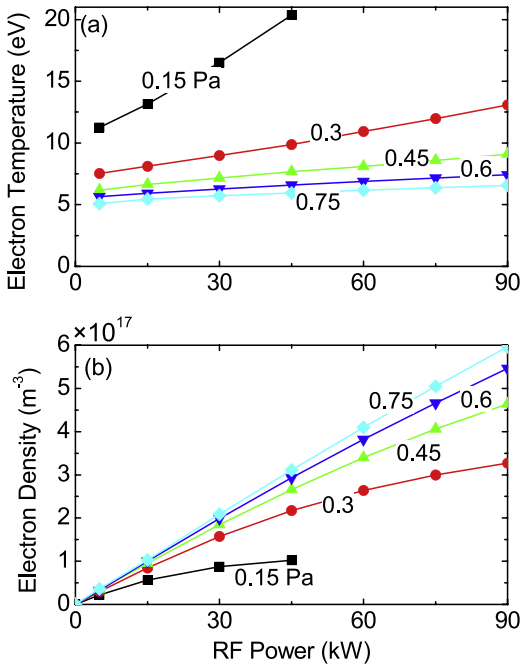

Figure 11. Electron density and temperature averaged over the ion source volume. 2D DSMC model for neutral transport, 2D fluid model of the plasma without magnetic filter field.

explained by a global model. Assuming steady-state conditions, the total amount of particles created through ionization in the ion source volume at a given time is equal to the number of particles lost on the device walls,

$$n_s u_B S = n_g k_i \langle n \rangle V, \tag{24}$$

where n_s is the plasma density at the sheath edge, $\langle n \rangle$ is the average plasma density ($n_e = n_i$ is assumed), $u_B = \sqrt{eT_e/m_i}$ is the Bohm velocity, m_i is the mass of H_2^+, $k_i(T_e)$ is the ionization rate (which is a function of the

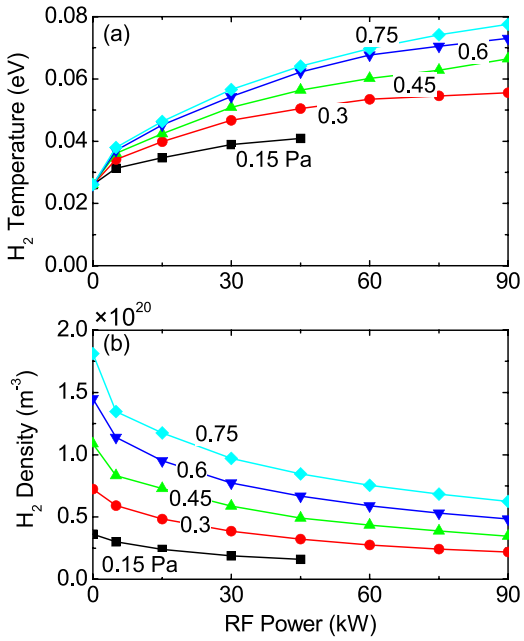

Figure 12. Molecular hydrogen density and temperature averaged over the ion source volume. 2D DSMC model for neutral transport, 2D fluid model of the plasma without magnetic filter field.

electron temperature), n_g is the background gas density and $S\,(V)$ is the ion source wall surface area (volume), respectively. Equation (24) is derived from the volume integration of the electron continuity equation. The term on the left-hand side (lhs) corresponds to the electron flux impacting the ion source walls and the rhs term is the volume integrated ionization rate. If the neutral gas density n_g is fixed then equation (24) provides an average estimate for the electron temperature that is independent of power. The electron temperature is linked to the ion source geometry through the surface-to-volume ratio S/V. An estimate for the average plasma density may be deduced from the power balance equation, that is, the power absorbed (P_{abs}) in the ion source volume is equal to the power lost on the walls,

$$P_{abs} = n_s u_B \varepsilon_T S, \tag{25}$$

where $\varepsilon_T\,(T_e)$ is the average energy lost per electron–ion pair lost on the walls [15, 21, 27]. For a given value of the background gas density n_g, the electron density hence increases linearly with the absorbed power. The gas density does vary with power as shown in figure 12 because of increased gas temperature and ionization rate as the absorbed power is increased. For instance at 0.75 Pa and 90 kW the gas density is depleted by ~65% compared to the density without discharge.

The charged particle balance in equation (24) provides a relation between the gas density and electron temperature, $n_g = u_B/(k_i d_{eff})$ where $d_{eff} = V/(hS)$ and $h = n_s/\langle n\rangle$. This relation can be calculated from the hydrogen ionization cross-section assuming a Maxwellian electron velocity distribution function, and the corresponding curve is shown on figure 13 (dark solid line). The results from the 2D model are also plotted (symbols) on the same figure. The symbols correspond to different gas pressures before the plasma is on, and, for the same symbol, the set of points correspond to several values of the discharge power (leading to distinct values of the averaged gas density due to the depletion associated with gas heating and ionization). We see on this figure that the 2D model results are in excellent agreement with the simple 0D model. High electron temperatures correspond to low gas densities and the asymptotic behavior of the curve at high electron temperatures shows that the discharge cannot be sustained below a given gas density (low gas pressure and high power). The good agreement between the simple 0D model (taking into account only H_2^+ ions) and the more complex 2D model with plasma chemistry may seem surprising but is due to the fact that ionization of molecular hydrogen is on the average significantly larger than ionization of atomic hydrogen. Also, in this plot, the neutral depletion is a parameter in the 0D model while it is self-consistently calculated in the 2D model.

The gas density variations with power are displayed in figures 12(b) and 14(b) for different pressures (the plotted densities are averaged over the whole ion source volume). The atomic hydrogen density increases with power because the dissociation rate increases with increasing plasma density and electron temperature while the H_2 density decreases with power because of gas heating and dissociation. However, the average H density reaches a limit when the power increases, because of the increase in the hydrogen atom temperature. The variations with power and pressure of the volume averaged molecular and atomic hydrogen temperatures are shown in

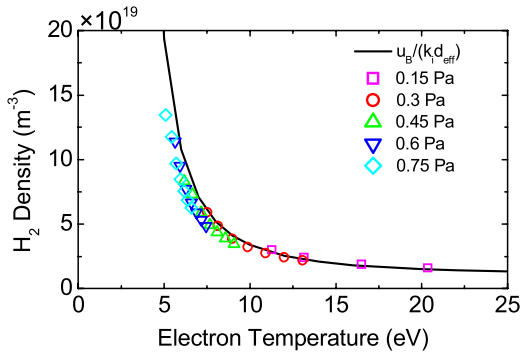

Figure 13. Average gas density versus the electron temperature. The black solid line is obtained with a 0D model (see text) while the symbols are from the 2D models, for different values of the initial gas pressure and absorbed power. 2D DSMC model for neutral transport, 2D fluid model of the plasma without magnetic filter field.

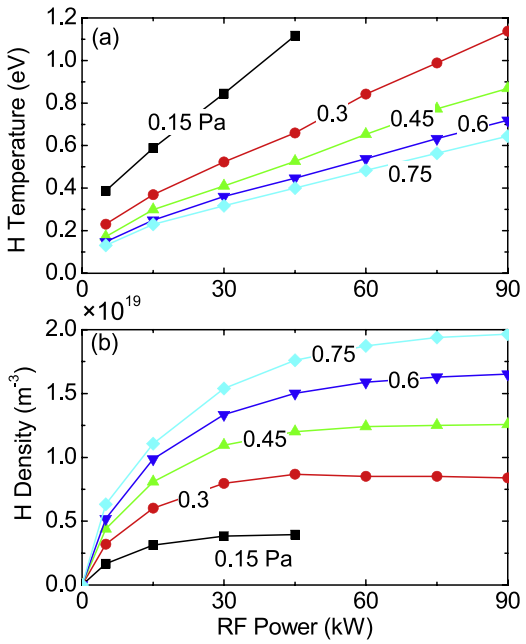

Figure 14. Atomic hydrogen density and temperature averaged over the ion source volume. 2D DSMC model, no magnetic filter field.

figures 12(a) and 14(a). The H temperature (in the 0.1–1.2 eV range) is much larger than the H_2 temperature (on the order of 0.02–0.08 eV). Both temperatures increase continuously with power. It is interesting to note that, for a given input power, the H temperature increases with decreasing pressure while the opposite is true for H_2. This is due to the larger energy exchange rate (between H and H_2) at higher pressure. The large H temperature is due (1) to the fact that H atoms are generated with a large energy during electron impact dissociation of H_2 and (2) to the generation of fast atoms at the walls resulting from the recombination of positive ions.

The wall accommodation coefficients are unknown experimentally. The model may be used to evaluate its influence on the plasma properties. Assuming that the neutral hydrogen particles are backscattered off the walls with the same temperature as the surface (accommodation of 1) for the reactions # 2, 4, 6 and 8 of table 3 instead of $\gamma = 0.5$, we find that (1) the amplitudes of the molecular hydrogen temperature and density are only slightly modified while (2) the H atom temperature is on average divided by 5 and the density as a consequence is larger by a factor of 2. The relationship between the accommodation coefficient and the neutral atom temperature is almost linear. The calculation was performed for a background gas pressure of 0.3 Pa and an absorbed power of 60 kW. There is experimental evidence that the temperature of H atoms is significantly larger than that of H_2 but the strong dependence of the H temperature on the accommodation coefficients demonstrated by the simulations shows that systematic comparisons of experiments and model results on the H temperature would be useful to get a better estimation of the accommodation coefficient.

4.2. Negative ion production on the cesiated PG surface

The non-Maxwellian flux of hydrogen atoms impacting the PG is $\Gamma_H \simeq 2.4 \times 10^{22}$ m^{-2} s^{-1} in the model for a 60 kW absorbed power, 0.3 Pa background hydrogen gas pressure, a magnetic filter field with a maximum of 15 G near the PG ($h_B = \mu_e B \gg 1$) and a PG bias voltage of 10 V. Seidl *et al* [46] have calculated the averaged conversion yield $\langle Y \rangle (T_H)$ for a Mo/Cs surface with dynamic cesiation assuming that the distribution function of the atomic specie was Maxwellian. The experiments were not performed in a plasma. In our case, the distribution function is highly non-Maxwellian and hence a range for the yield may be estimated either by (1) fitting the energy distribution function of the atoms with a Maxwellian distribution,

$$\langle Y \rangle = R_N \eta_0 \exp\left(-\frac{E_{th}/R_E}{T_H}\right), \tag{26}$$

where $T_H \simeq 0.8$ eV in the vicinity of the PG in the model (figure 10) or (2) considering the atoms as a 'beam',

$$YE_{in} = R_N \eta_0 (E_{in} - E_{th}/R_E). \tag{27}$$

In both cases, $R_N \eta_0 = 0.42$ and $E_{th}/R_E = 1.05$ eV is assumed [46] (deduced from the experiments). E_{in} is the incident energy of the atom. Using equation (26), we find $\langle Y \rangle \simeq 11.5\%$ and hence $j_G \simeq 430$ A m^{-2} while equation (27) gives $Y \simeq 18\%$ and $j_G \simeq 690$ A m^{-2}. j_G is the negative ion current density generated on the PG surface.

5. Plasma transport across the magnetic filter

In this section, we model the plasma properties of the (one driver) ITER-prototype negative ion source at BATMAN with a 2.5D PIC-MCC algorithm (section 2.1.3) using a density scaling of $\alpha = 400$ (plasma density 400 smaller than in the real source). We describe not only the plasma transport across the filter, but also the extraction of negative ions, considering a limited number of grid apertures (slits). Although care must be taken in the interpretation of the results on negative ion extraction with such a large density scaling, we think that these results are interesting because plasma source and negative ion extraction are described in the same model (extraction models are generally performed on a simulation domain around a single aperture, and the correctness of the boundary condition inside the simulated plasma region is currently an issue [60]).

The magnetic filter field profile is Gaussian following equation (19) with $B_0 = 75$ G, $L_m = 8$ cm and $x_0 = 39$ cm. We model the XZ plane, as shown in figure 3(b) and the magnetic field is directed along (OY). The length of the third, un-simulated dimension, is $L_y = 32$ cm (also for the discharge). The numerical resolution is 1024×1536 grid nodes with ~100 ppc and we model a lower plasma density, that is, $\langle n_p \rangle = 7.5 \times 10^{14}$ m^{-3}. We simulate 7 slit apertures in the PG, each with a diameter of 1.5 cm and length $L_y = 32$ cm. The deflection magnetic field $\mathbf{B}_D$ is calculated with a third-party code [53]. Lastly, we consider an absorbed power of 60 kW and a background gas pressure of 0.3 Pa. The external RF power is coupled to the plasma in the model by artificially heating macroparticles in the driver region following the method described in section 2.1.4 ($\nu_H = 10^8$ s^{-1}). Plasma particle species are electrons, negative ions H^- and positive ions (protons, H_2^+ and H_3^+ ions). The physical-chemistry is summarized in tables 1 and 2. The neutrals are not modeled and a constant density and temperature profile is implemented instead with $n_{H_2} \simeq 4 \times 10^{19}$ m^{-3}, $T_{H_2} \simeq 0.1$ eV (figure 12), $n_H \simeq 10^{19}$ m^{-3} and $T_H \simeq 1$ eV (figure 14), respectively. The latter are consistent with experimental observations [47]. Negative ions are produced inside the ion source volume (reaction #17 of table 1) and on the cesiated PG surface either as a byproduct of positive ion impacts or atomic hydrogen. We assume a negative ion current density of $\alpha j_G = 600$ A m^{-2} generated by H atoms and an ion temperature of $T_n = 1$eV.

5.1. Plasma asymmetry

Figure 15 shows the electron density in (a) and (b), electron temperature (c) and plasma potential profiles (d) in the plane perpendicular to the magnetic field lines (XZ plane) of the BATMAN negative ion source. The PG bias voltage is 25 V in (a), 20 V in (b)–(d). The Hall effect (section 3) generates an electric field directed downward and hence the transverse potential profile is asymmetric. The plasma density is highest in the vicinity of the top wall of the ion source, i.e., where the plasma potential is maximum (the maxima is shifted up compared to a situation without a magnetic field). The extent of the plasma asymmetry is strongly related to the PG voltage [12, 24] (biased positively with respect to the ion source walls). A larger electron current is drawn from the driver through the filter when the bias is increased and hence the Hall electric field is strengthened. The temperature profile is also asymmetric (oblique isothermals) due to the magnetized electron drift dynamics which evolve into an oblique electron flux across the magnetic filter. $T_e \simeq 10$eV in the discharge region and ~1.5 eV in the vicinity of the PG. Lastly, the densities of the plasma particle species averaged over the ion source volume are $\alpha \langle n_e \rangle \simeq 2.9 \times 10^{17}$ m^{-3}, $\alpha \langle n_n \rangle \simeq 9 \times 10^{15}$ m^{-3} (negative ion density), $\alpha \langle n_{H_3^+} \rangle \simeq 6.5 \times 10^{16}$ m^{-3} and $\alpha \langle n_{H_2^+} \rangle \simeq \alpha \langle n_{H^+} \rangle \simeq 1.17 \times 10^{17}$ m^{-3}, respectively.

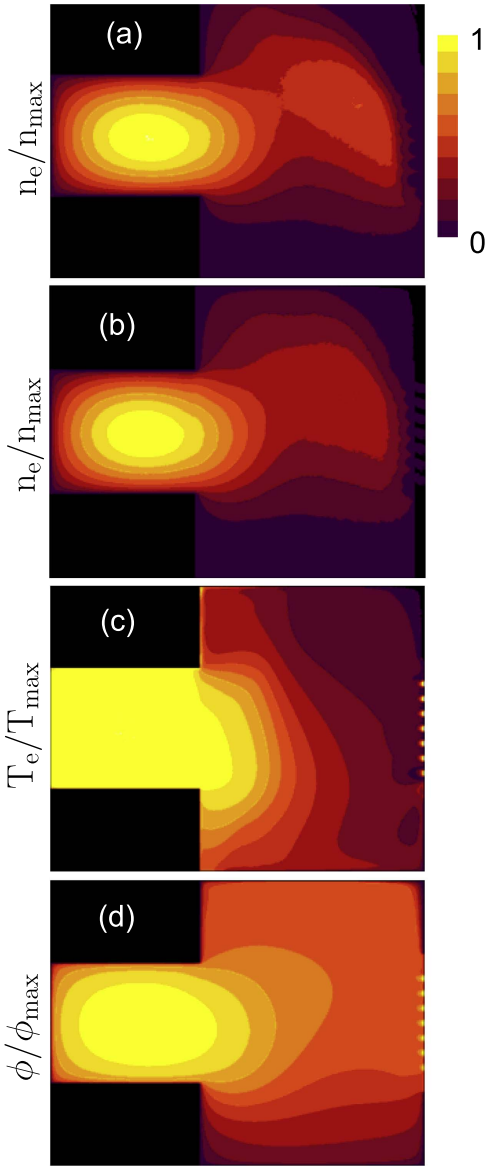

Figure 15. Normalized electron density (a)–(b), electron temperature (c) and plasma potential profiles (d) in the XZ plane of the ITER prototype ion source at BATMAN (figure 3) calculated by the 2.5D PIC-MCC model. The simulation parameters are a 60 kW absorbed power, 0.3 Pa, a numerical grid resolution of 1024 $\times$ 1536 nodes, ~100 ppc and a scaling factor $\alpha = 400$ (corresponding to a plasma density averaged over the whole simulation domain of $\langle n_p \rangle \simeq 3 \times 10^{17}/\alpha$ m^{-3}). The PG bias voltage is 25 V in (a), 20 V in (b)–(d). Lastly, $n_{max} = 1.2 \times 10^{18}/\alpha$ m^{-3}, $T_{max} = 10$ eV and $\phi_{max} = 40$ V.

5.2. Negative ion dynamics

Figure 16 shows the negative ion flux (a) and density (b) profiles in the XZ plane of BATMAN. The PG bias voltage is 20 V. The flux corresponds solely to negative ions produced on the PG by neutral atom impacts. The numerical resolution is 1024 $\times$ 1536 nodes with ~35 ppc. The scaling factor is $\alpha = 400$. Streamlines are displayed in figure 16(a) to indicate the direction of the negative ion flux. Except close to the PG, the flux is directed toward the ion source volume. Negative ions which are extracted originate consequently from the PG surface surrounding the apertures. Negative ions are somewhat magnetized, which significantly enhance the skewness of the density profile displayed in figure 16(b). The negative ions drift toward the top wall. The average kinetic energy about 2 cm from the PG is $\langle E_k \rangle \simeq 1.3$ eV translating into a Larmor radius of $r_L \simeq 2.2$ cm with $|\mathbf{B}| \simeq 75$ G. The shortest mean-free-path for the negative ions corresponds to the charge exchange collisions with atomic hydrogen (reaction #17, table 2). We find $\lambda_{CEX} \simeq 6$ cm near the PG (~2 cm). The ions are hence magnetized, $r_L/\lambda_{CEX} < 1$. Other mean-free-paths are $\lambda_{DES} \simeq 40$ cm for the destruction (sum of the reactions #16 of table 1, #10, #11, #14, #15 and #16 of table 2, respectively) and $\lambda_{EL} \simeq 20$ cm for the elastic collisions with neutrals (reactions #12 and #13 of table 2). The negative ion density averaged over a line-of-sight (LOS) parallel to the PG (from the top to the bottom wall) and 2 cm from the latter is $\alpha \langle n_n \rangle \simeq 6.5 \times 10^{16}$ m^{-3} which is of the order of experimental measurements [12]. At the same distance from the PG, the negative ion density

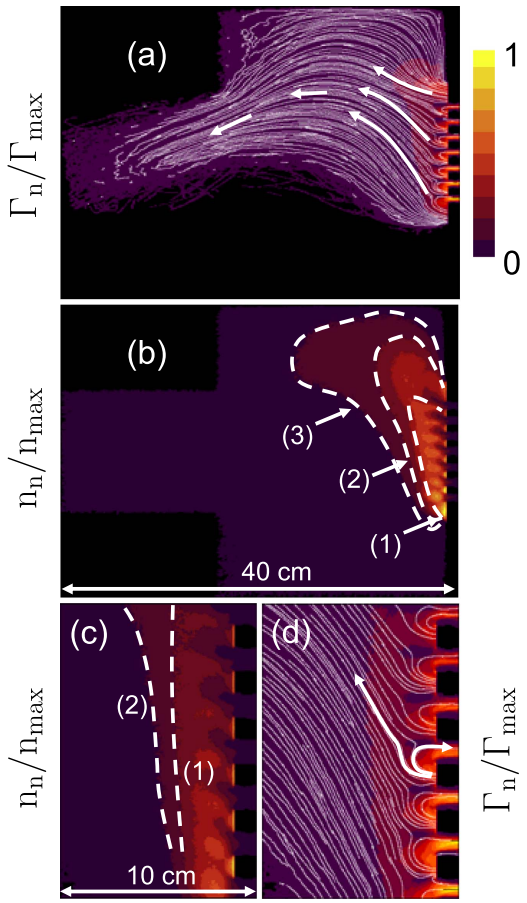

Figure 16. Normalized negative ion flux (a) and density (b) profiles in the XZ plane of the ITER prototype ion source at BATMAN. A zoom in the vicinity of the PG is shown in (c) for the density and (d) for the flux. 2.5D PIC-MCC model, 60 kW absorbed power, 0.3 Pa, a numerical grid resolution of 1024 × 1536 nodes, ~35 ppc and a scaling factor $\alpha = 400$. The PG bias voltage is 20 V, $n_{max} = 2.8 \times 10^{17}/\alpha$ m^{-3} and $\Gamma_{max} = 4 \times 10^{21}/\alpha$ m^{-2} s^{-1}. The flux in (a) and (b) corresponds to negative ions produced on the PG by neutral atom impacts. The arrows (white color) show the direction of the flux. The dashed lines are isocontours corresponding to $\alpha n_n = 10^{17}$ m^{-3} in (1), 5×10^{16} m^{-3} (2) and 3×10^{16} m^{-3} (3).

averaged over the width of the grid is $\alpha n_n \simeq 1.3 \times 10^{17}$ m^{-3} while $\alpha n_e \simeq 1.7 \times 10^{17}$ m^{-3}. Lastly, a negative ion current of $\alpha j_G = 600$ A m^{-2} produced on the PG is space charge saturated and a virtual cathode forms in the plasma sheath in front of the electrode surface (the plasma potential presents a minimum which limits the extracted negative ion current). The depth of the virtual cathode is $\phi_c \simeq -1$ V in the model and hence the saturation current (corresponding to the ion current which escapes the PG surface) is $j_{sat} = j_G \exp(-|\phi_c|/T_n) \simeq 220/\alpha$ A m^{-2} for a Maxwellian flux distribution function [49]. Note that the probability for a negative ion produced on the PG to be extracted from the ion source is on the order of 50% for a PG bias voltage of 20 V.

The asymmetry in the plasma parameters has important consequences on the (extracted) negative ion beamlet profiles. The beamlet currents may deviate by as much as 50% from the average current in the model. The ITER accelerator has a ±10% acceptance and this may likely translate into some beam interception on the accelerator grids.

5.3. Electron and negative ion extraction versus the PG bias voltage

Figure 17 shows the electron and negative ion current extracted from the 7 slit apertures of diameter 1.5 cm versus the PG voltage. The EG potential is set to $V'_{EG} = 210$ V. This value is obtained by assuming that the extracted currents scale with the Child–Langmuir law $\alpha j_n = \mu V_{EG}^{3/2}$ in order to estimate the EG voltage for a plasma density $\alpha = 400$ times smaller than the value encountered in the actual ITER prototype ion source at BATMAN. This approximation will be further discussed in section 7. μ is the perveance and V_{EG} is the potential for $\alpha = 1$. We find $V'_{EG} = V_{EG}/\alpha^{2/3}$ assuming $V_{EG} = 11.4$ kV on the EG, which is located 9 mm from the back of the PG in the model (this corresponds to a potential $V_{EG} \simeq 7.5$ kV for the 6 mm gap of the ITER accelerator). The other parameters of the simulation are identical to the ones of the preceding section.

The positive ion flux on the PG decreases with a larger bias voltage [22] which has two consequences: (1) the negative ion current produced on the PG by positive ion impacts decreases as well and (2) a smaller positive ion

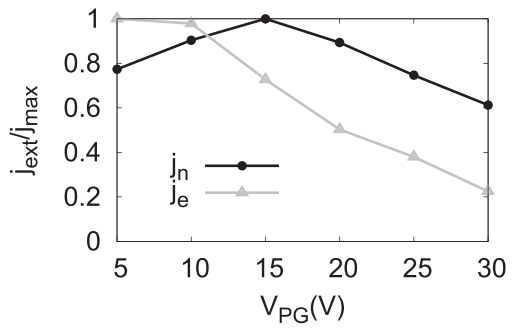

Figure 17. Normalized extracted electron and negative ion current versus the PG bias voltage. The extraction grid voltage is $V'_{EG} = 210$ V and $\alpha = 400$. The PG is floating for $V_{PG} = 20$ V.

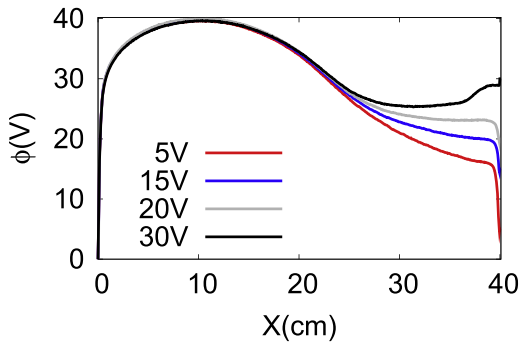

Figure 18. Axial plasma potential profile between two apertures versus the PG bias voltage. $V'_{EG} = 210$ V and $\alpha = 400$.

density in the Debye sheath results in a larger virtual cathode depth ϕ_c. The latter reduces the magnitude of the negative ion current density escaping the PG (j_{sat}). The PG bias voltage changes also the shape of the plasma potential in the vicinity of the apertures as shown in figure 18. The potential profile flattens with an increasing bias voltage until the PG is floating (i.e., an equal amount of positive and negative charges are impacting the grid). The PG is floating for $V_{PG} = 20$ V in the model (~5% of the extracted negative ions are produced by positive ions). The flattening of the plasma potential greatly enhances the residence time of the negative ions in the extraction region and beside a lower saturation current j_{sat}, the extracted negative ion current increases with the PG bias up to a floating PG (figure 17). For $V_{PG} > 20$ V, the amplitude of the plasma potential is gradually getting lower than the applied bias voltage everywhere parallel to the PG. Negative ions are hence increasingly trapped near the PG surface and the extracted current is dropping as shown in figure 17. The potential in the pre-sheath 1 cm from the PG is 1.2 V below the electrode voltage for $V_{PG} = 30$ V in figure 18. This behavior is confirmed by experimental measurements [12]. Lastly, the gap between the plasma potential at the edge of the Debye sheath in front of the PG and the bias voltage (V_{PG}) decreases with a larger value of the bias (figure 18). The Electron temperature in the extraction region is $T_e \simeq 1.5$ eV in the model and consequently more electrons may cross the sheath barrier (and be collected on the PG surface). This explains the continuous drop of the co-extracted electron current versus the PG bias voltage shown in figure 17.

5.4. Summary

Although they have been obtained with a large scaling factor, the results presented in this section raise some questions about the plasma asymmetry in the source and its possible consequences on the non-uniform distribution of the extracted negative ion current along the PG surface. They show that drawing an electron current across the magnetic filter in a fusion-type negative ion source induces a plasma asymmetry due to the Hall effect (the plasma asymmetry is confirmed by experiments as described in the next section). As a consequence, the extracted negative ion beamlet current density is asymmetric as well in the model, with values exceeding the ±10% current spread foreseen for the ITER NBI electrostatic accelerator. In addition, we found that the PG bias voltage (1) enhances the plasma asymmetry (figures 15 and 16), (2) increases the extracted negative ion current up to (approximately) a floating PG and lastly, (3), induces a monotonous decrease of the co-extracted electron current (figure 17). The extracted particle currents and the plasma potential profiles were derived from a fixed value of the plasma density (scaling factor $\alpha = 400$). Only the PG bias potential was varied

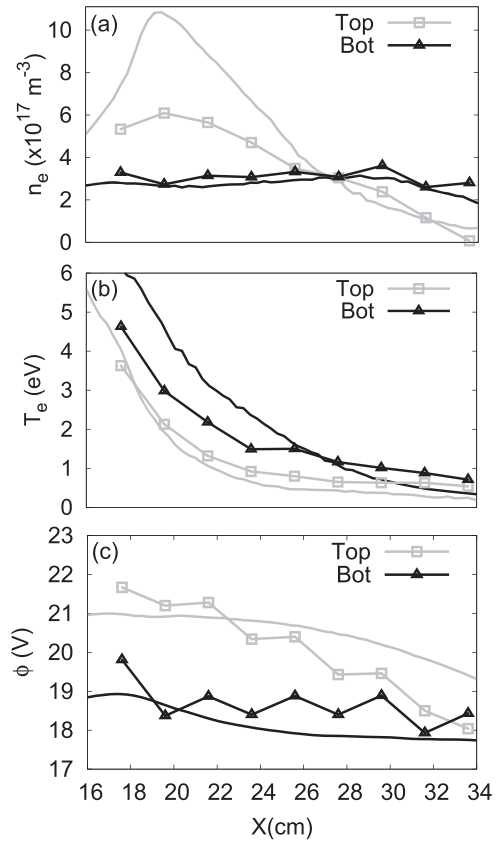

Figure 19. Axial electron density, temperature and plasma potential profiles for two Langmuir probe positions along (Oz), that is, $z = -10$ cm (bottom) and $z = 10$ cm (top). Both probes are positioned at $y = -5$ cm. The experimental data of Schiesko *et al* [62, 63] are indicated by the symbols (square and triangles). The experimental conditions correspond to a background hydrogen gas pressure of 0.6 Pa, a RF power of 40 kW and a magnetic filter field generated by permanent magnets on the side walls of the ion source, 9 cm from the PG.

in the simulations. The profiles strongly resemble experimental measurements [12, 61] which seems to indicate that the conclusions drawn from this section may be extrapolated to higher plasma densities.

6. Comparison with experiments

In this section, we compare the model to experimental measurements. We simulate the conditions reported in Schieko *et al* [62]. The model is a 3D PIC-MCC algorithm with a numerical resolution of $128 \times 96 \times 192$ grid nodes, a scaling factor $\alpha = 5 \times 10^4$ and 20 ppc. The magnetic filter field is generated by permanent magnets, positioned against the lateral wall of the BATMAN prototype source and 9 cm for the PG. The simulation domain is displayed in figures 3(a) and (b). The discharge is approximated as a rectangular box in the model instead of a cylinder. The filter field map is calculated by a third party software [53]. The background hydrogen gas pressure in the experiment was 0.6 Pa and the RF power $P_{\mathrm{RF}} = 40$ kW. The properties of the neutrals are unknown experimentally and we implemented the values derived from the DSMC model (figures 12 and 14), i.e., a molecular hydrogen density of $n_{\mathrm{H_2}} = 9 \times 10^{19}$ m^{-3}, temperature $T_{\mathrm{H_2}} = 0.07$ eV, atomic hydrogen density $n_{\mathrm{H}} = 10^{19}$ m^{-3} and temperature $T_{\mathrm{H}} = 0.3$ eV, respectively. The PG bias voltage is set to $V_{\mathrm{PG}} = 18.5$ V [63] and we assumed an absorbed power of 15 kW. The conversion yield for hydrogen atoms on a cesiated PG surface is derived from equation (26). We find $\langle Y \rangle \simeq 1.3\%$ for $T_{\mathrm{H}} = 0.3$ eV which translates into a negative ion current produced on the PG of $j_G \sim 50$ A m^{-2} (this is about 12 times smaller than for a pressure of 0.3 Pa). The latter corresponds to an optimal cesiation of the PG. Lastly, we assumed that $T_{\mathrm{n}} \simeq T_{\mathrm{H}}$. Figure 19 shows the axial profile for the electron density, temperature and plasma potential for two Langmuir probe positions along (Oz), that is, $z = -10$ cm (bottom) and $z = 10$ cm (top). Both probes are positioned at $y = -5$ cm. The experimental data [62, 63] are plotted in figure 19 for comparison. Both the experiment and the 3D PIC-MCC model exhibit similar features. The magnetic filter field generates an asymmetry in the plasma parameters (the gap in the plasma potential is the hallmark of the Hall effect). The main discrepancy between the experiments and the model comes from the external power (we assumed 15 kW of *absorbed* power versus 40 kW of RF power in the experiments). The peak for the electron density near the exit of the driver is also more pronounced in the

model. This may be due to the oversimplifying assumption of implementing a rectangular geometry for the discharge. The scaled electron Debye length is $\bar{\lambda}_{De} \simeq 6.5$ mm on average in the calculation. The fraction of the volume occupied by the plasma sheath is $2L_{sh}/L_s \sim 15\%$, where $L_s = \sqrt[3]{V_s} = 37$ cm with V_s the ion source volume and $L_{sh} \sim 4\bar{\lambda}_{De}$ the size of the sheath. The numerical resolution is similar to the example shown in section 3.2 for an average plasma density of $\langle n_p \rangle = 2.5 \times 10^{13}$ m^{-3} (figure 6).

7. Extraction of negative ions

In this section, we simulate the extraction of negative ions from a fusion-type ion source using a model which is restricted to a single aperture [60]. The simulation domain is shown in figure 3(c).

7.1. Numerical issues

Recently published results from PIC-MCC models [64–66] have led to a counter-intuitive and unexpected description of negative ion extraction. Using chamfered apertures in the simulations, the models [64, 66] show that only those negative ions emitted from the tip of the chamfered aperture can be extracted, which is rather surprising and does not seem to correspond to a proper operation of the extraction system. A very small negative ion current is emitted from the rest of the grid surface due to space charge saturation associated with very large values of the potential drop in front of the emitting surface (i.e., a virtual cathode). The numerical grid spacing used in the simulations was much larger than the Debye length (typically by a factor between 5 and 10). Experiments, on the other hand, have shown that extraction of a negative ion beam from a plasma electrode with a flat surface around the aperture is actually possible [5, 67, 68]. We show in section 7.3 that a grid spacing smaller than the Debye length is required for a proper description of the plasma in the vicinity of the PG (including the shape of the virtual cathode) [69]. We describe in section 7.4 the properties of the plasma meniscus predicted by the model. Lastly, we discuss the use of scaling laws in a 2D model of negative ion extraction (slit apertures) in sections 7.4 and 7.5, i.e., we compare the real plasma density ($\alpha = 1$) to lower densities ($\alpha > 1$) and analyze the correlations. An extrapolation to circular apertures (3D PIC-MCC modeling) is also discussed.

7.2. Model

The simulation domain is described in figure 3(c). The model is a zoom around a single aperture of dimensions 3.2×1.6 cm^2 in 2D. The aperture (slit) is not chamfered and with a diameter of 8 mm as in the prototype ion source at BATMAN described in [5]. The top and bottom boundaries are periodic while all the others are of Dirichlet type. The PG is set at a given reference potential (0 V in our case) and the left-hand side (lhs) boundary voltage V_{LB} is adjusted in order to simulate the effect of a bias potential. The plasma is numerically sustained by re-injecting an electron-positive ion pair for each positive ions lost on the walls of the simulation domain. Particles are re-injected on the lhs of the domain between $x = 2$ and 4 cm and the electron temperature is maintained by replacing the macroparticle velocity by a new one sampled from a Maxwellian distribution at a preset temperature $T_e = 2$ eV. Negative ions are uniquely produced on the PG surface (we specifically want to assess the dynamics of negative ions which are produced on the electrode). The physical chemistry is simplified. We only consider negative hydrogen ions, H_2^+ and electrons (reactions #14 and #15 of table 2 have a negligible contribution). We implemented a background gas density $n_{H_2} = 4 \times 10^{19}$ m^{-3}, temperature $T_{H_2} = 0.1$ eV and an atomic hydrogen density of $n_H = 10^{19}$ m^{-3} with $T_H = 1$ eV, respectively. The positive ion temperature is $T_p = 2$ eV. The magnetic filter field profile is assumed constant with $B_z = 75$ G and the cusp field from the suppression magnets B_D is derived from an analytical formulation,

$$B_x = B_0 \sin\left(\frac{\pi y}{d}\right) \exp\left[\frac{-\pi (x_R - x)}{d}\right], \tag{28}$$

$$B_y = B_0 \cos\left(\frac{\pi y}{d}\right) \exp\left[\frac{-\pi (x_R - x)}{d}\right], \tag{29}$$

where $x_R = 3.2$ cm is the position of the EG, $d = 1.6$ cm is the distance between magnet bars and lastly $B_0 = 600$G for the BATMAN configuration.

7.3. Convergence

Figure 20 shows the transverse virtual cathode potential profile (at its minimum), parallel to the PG, versus the numerical grid spacing ($\Delta x = \Delta y$) in the model. The latter is varied between $\Delta x = 250$ μm ($\Delta x/\langle \lambda_{De} \rangle \simeq 6$) down to $\Delta x = 21.3$ μm ($\Delta x/\langle \lambda_{De} \rangle \simeq 0.5$), where $\langle \lambda_{De} \rangle$ is the electron Debye length averaged over the whole simulation domain. The average plasma density in the calculation is $\langle n_p \rangle = 6 \times 10^{16}$ m^{-3} and $V_{LB} = -5$ V. The virtual cathode profile converge for a grid spacing of the order of the Debye length (or below) [16, 17]. For

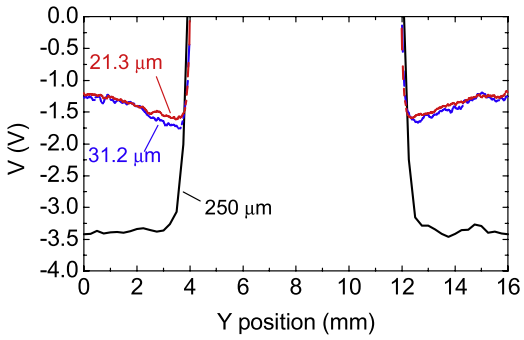

Figure 20. Transverse virtual cathode potential profile (parallel to the PG) versus the numerical grid spacing ($\Delta x = \Delta y$) in the model. $\Delta x/\langle\lambda_{De}\rangle \simeq 6$ for $\Delta x = 250$ μm where $\langle\lambda_{De}\rangle$ is the electron Debye length averaged over the entire simulation domain.

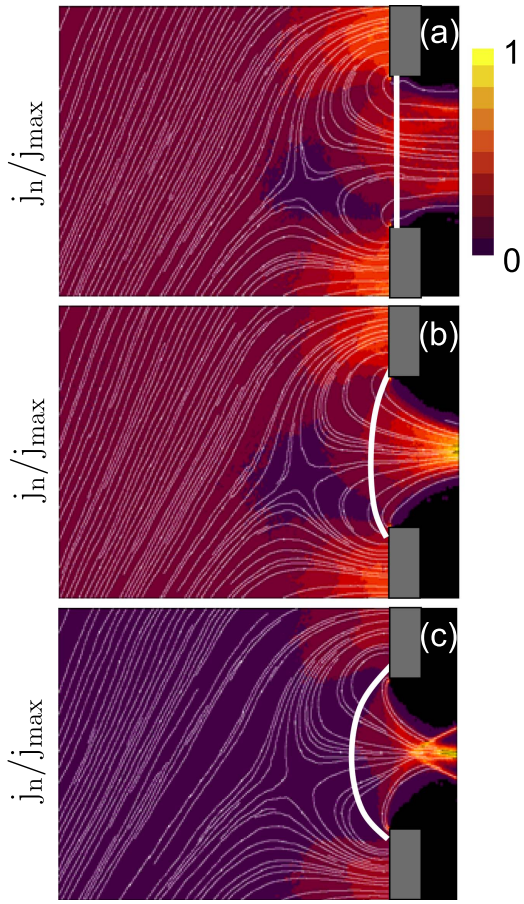

Figure 21. Normalized negative ion current density profile versus the extraction grid potential V'_{EG}. The model is a 2D PIC-MCC algorithm with slit apertures. The average plasma density in the simulation domain is $\alpha\langle n_p\rangle = 3 \times 10^{17}$ m^{-3} with $\alpha = 4$. $V'_{EG} = 450$ V in (a), 900 V in (b) and 1800 V in (c), respectively. The meniscus profile is highlighted in white.

$\Delta x/\langle\lambda_{De}\rangle \gtrsim 1$, numerical heating increases the electron temperature which in turn modifies the plasma parameters. The virtual cathode depth drops in the model and the negative ion saturation current escaping the PG is hence also significantly reduced.

7.4. Beam characteristics versus the extraction potential

Figure 21 shows the normalized negative ion current density profile versus the EG potential for $V'_{EG} = 450$ V in (a), 900 V in (b) and 1800 V in (c), respectively. The model is a 2D PIC-MCC algorithm with slit apertures. The average plasma density in the simulation domain is $\alpha\langle n_p\rangle = 3 \times 10^{17}$ m^{-3} with $\alpha = 4$. $V_{LB} = 0$ V. The numerical resolution is 1024 × 512 grid nodes with 100 ppc. The meniscus, defined as the boundary where the quasi-neutrality is no longer fulfilled, is highlighted in white. The meniscus recedes toward the plasma volume

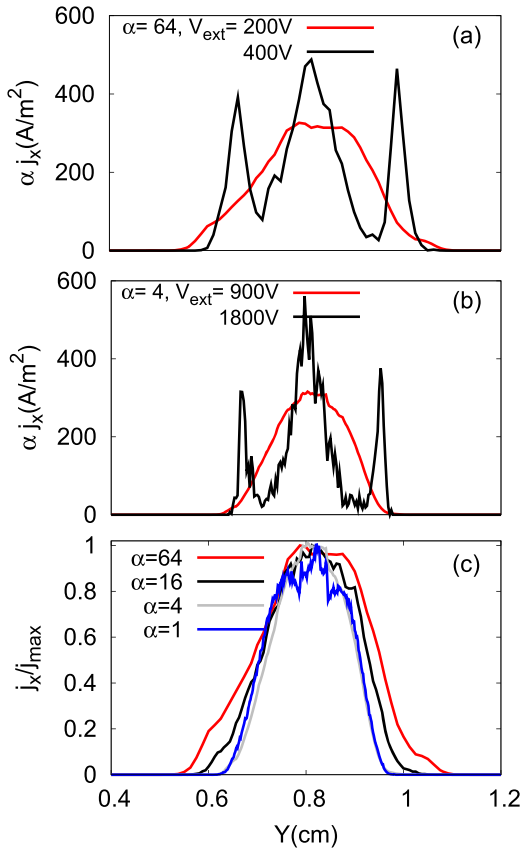

Figure 22. Transverse negative ion current density profile on the EG grid versus the extraction voltage and the plasma density. The average plasma density in the calculation is $\alpha \langle n_p \rangle = 3 \times 10^{17}$ m^{-3} with α ranging from $\alpha = 1$ to 64. $V'_{EG} = 200$ V in (a) and 900 V in (b) correspond to plasma meniscus with similar curvature radius. $r_c/a \gg 1$.

when the EG potential is increased and below a curvature radius $r_c \lesssim a$ (where $2a = 8$ mm is the diameter of the aperture), aberrations appears in the extracted negative ion beam.

7.5. Scaling laws

Both the extraction (EG) voltage and the plasma density affect the shape of the virtual cathode (the capability of the plasma to screen off the external potential is related to the electron Debye length). The EG potential modifies the amplitude of the plasma potential in the extraction region (it acts similarly to a bias voltage applied on the PG). The trajectories of the charged particles in the vicinity of the aperture are hence altered and the virtual cathode depth is in turn impacted. The latter is increasing (in absolute value) with the extraction potential. This induces a drop of the extracted negative ion current as well. In order to derive scaling laws, i.e., to correlate the plasma properties between high versus low plasma densities, we must preserve the curvature radius of the meniscus. One approximate solution is to calculate the extraction potential with the Child–Langmuir law,

$$V'_{EG} = V_{EG}\left(\frac{I'_n}{I_n}\right)^{2/3}, \tag{30}$$

where the extracted negative ion currents have hence been retained (primes denote the voltage and current for $\alpha > 1$). Figure 22 shows the negative ion current density profile along (OY) on the EG versus the EG potential and the plasma density. $V'_{EG} = 200$ V in (a) and 900 V in (b) correspond to plasma meniscus with nearly identical curvature radius ($r_c/a \gg 1$). In both cases, doubling the extraction potential induce the appearance of aberrations in the extracted ion beam profile ($r_c/a \sim 1$). The profiles displayed in figures 22(a) and (b) are very similar beside a factor 16 in plasma density. This shows the capability of the model to reproduce correctly the beam dynamics with lower densities. This is also visible in figure 22(c) which shows the beam profiles for the same meniscus curvature radius ($r_c/a \gg 1$) and for a density ranging from $\alpha = 1$ to 64. The numerical resolution is 2048 × 1024 (256 × 128) grid nodes for $\alpha = 1$ ($\alpha = 64$), respectively, and 40 ppc. $V_{LB} = 0$ V. The extracted negative ion current varies by a factor 2 (scaling factor) between $\alpha = 1$ and 64 while the virtual cathode depth by a ratio of ~1.6. The latter may be used to estimate the negative ion current density extracted from circular apertures instead of slits. The only modification in the model is the geometry of the extraction aperture and hence we posit that the scaling factors are preserved. The scaled negative ion current derived from a

3D PIC-MCC calculation is $j_n \simeq 100$ A m^{-2} associated with a (scaled) average virtual cathode depth of $\langle \phi_c \rangle \simeq -1.6$ V. We modeled an aperture radius of $r = 4$ mm, a width of 2 mm and a negative ion current emitted on the PG surface of $\alpha j_G = 600$ A m^{-2}. $V_{LB} = 0$ V and $V'_{EG} = 400$ V. The numerical resolution was 256×96^2 nodes with $\alpha = 64$. We did not model the mechanisms to either produce negative ions in volume via the dissociative attachment of the background gas molecules or from the impact of positive ions on the cesiated PG. Speth *et al* [5] reports that ~20% of the extracted ions (gas pressure of ~0.4 Pa for a RF power of ~100 kW) in BATMAN originated from volume processes. Adding this small correction to the numerical estimates gives $j_n \simeq 120$ A m^{-2}. This is to be compared to an experimental value of $j_n \simeq 140$ A m^{-2}. Note that a slight disparity in the virtual cathode profile between the model and the experiments translates into a significantly larger difference for the amplitude of the extracted negative ion current. The properties of the virtual cathode are unknown experimentally. In addition, the current model (a zoom around a single aperture with lateral periodic boundary conditions) neither account for the complex dynamics of the electrons resulting from the magnetic drifts inside the expansion chamber nor for the properties of the positive ions which are produced in the discharge and impact the PG with a high average energy [22]. Both will modify the characteristics of the virtual cathode. This question should be addressed in future work.

8. Conclusion

This paper proposes a synthesis, illustrated with new results, of the work that has been carried at LAPLACE on the modeling and simulation of the negative ion sources for the neutral beam injection systems used in fusion applications (ITER, DEMO). We can summarize the important results as follows.

- Fluid models coupled with the plasma chemistry and neutral flow in the negative ion source, show that the gas density is non-uniform in the chamber and is strongly depleted due to gas heating and ionization. Due to the low gas density, the properties of the plasma and gas phase are controlled not only by collisions in the volume but by interaction with the walls. For example, the recombination of high energy ions at the walls contributes to the generation of fast neutrals in the discharge chamber (the presence of high energy, i.e. up to 50 eV ions is due to the high plasma potential resulting from the low gas density). Moreover kinetic (DSMC) simulations of the neutral gas transport show that the velocity distribution function of neutral species is strongly non-Maxwellian, with a highly populated tail. This can certainly affect the production of negative ions on the PG surface. The fluid models of the plasma developed at LAPLACE are very useful and efficient to study the plasma properties with complex chemistry and neutral transport. They are however more difficult to use at high magnetic fields (problems with numerical accuracy and convergence) and are not adapted to the description of negative ion extraction.
- Particle (PIC-MCC) simulations are very powerful but due to constraints on the grid spacing and time step, cannot be used for the high plasma densities and large volume of the negative ion source. We have discussed in this paper how simulations performed under conditions of smaller plasma densities ('scaling'), although not 'exact', can provide a very useful insight in the physics of the source, and that the results can often be linearly extrapolated to the real densities with a good approximation. Care must however be taken when the sheaths play an active role in the discharge or in the simulation of negative ion extraction (and when instabilities and turbulence are present). One important conclusion of the 'scaled' PIC-MCC simulations is the demonstration that the presence of the magnetic filter can induce a strong asymmetry in the plasma properties in the direction parallel to the PG. This is because the diamagnetic and $\mathbf{E} \times \mathbf{B}$ drift in the magnetic filter region are not closed, as in closed-drift sources (Penning source, magnetron discharge, Hall thruster etc...) but are directed toward a wall. This induces a Hall effect which generates the plasma asymmetry and enhances electron transport though the filter. Calculations performed with a large scaling factor tend to show that the plasma asymmetry leads to a significant non-uniformity of the negative ion current density along the extraction apertures. The validity of linear extrapolation of this result to the real conditions of plasma density is difficult to prove but nevertheless, these simulations raise the question of beam uniformity.
- The description of negative ion extraction by PIC-MCC simulations is also difficult because of the high plasma densities and even if the simulation domain is limited to a small region around a grid aperture, with periodic boundary conditions. We have shown that erroneous and unphysical results can be obtained if the constraints imposed by the PIC method are not strictly taken into account. We have shown that the conclusion, drawn in some recent papers, that only a small negative ion current can be extracted from the PG surface facing the plasma due to space charge current limitation is highly questionable and is a consequence of a misuse of the PIC-MCC technique. 3D simulations respecting the constraints inherent to an explicit PIC simulation seem difficult to perform or to use for systematic parametric studies even for parallel computations on a large number of nodes. We believe that interesting and useful insight could be obtained from simulations with

scaled plasma densities and extraction voltages, although more work is needed to study how the results of simulations performed at lower plasma densities can be extrapolated to the real conditions.

Although the models presented in this paper bring an interesting and useful insight into the physics of negative ion sources and negative ion extraction, several questions must be addressed in future work to improve our qualitative understanding of the physics and the predicting capabilities of the models. Among them: (1) improvement of the boundary conditions mimicking the plasma flow in negative ion extraction models which are restricted to a sub-domain of the ion source volume near an aperture, (2) extraction of negatively charged particles versus the PG bias voltage, (3) assessment of the extracted beamlet asymmetry, (4) plasma properties in front of an aperture surrounded by a magnetic cusp. Effect of the cusp on the extraction of negative ions and electrons, role of secondary electron emission from the surface on electron extraction, (5) RF plasma coupling inside the ICP discharge. Incidence of the high RF power and low gas pressure on the particle kinetics (anomalous skin depth and ponderomotive effects), influence of a non-Maxwellian electron velocity distribution in the driver, (6) role of volume produced versus surface produced negative ions as a function of gas pressure, (7) impact of the ion source walls on the plasma characteristics (for instance, the relationship between the vibrational excitation of molecular hydrogen backscattering off the surfaces and production of negative ions in volume).

Finally we note that modeling should also play an important role in the research on alternative plasma sources for the neutral beam injection system of future reactors (e.g., DEMO) [70].

Acknowledgments

This work has been carried out within the framework of the EUROfusion Consortium and has received funding from the Euratom research and training programme 2014-2018 under grant agreement No 633053. The views and opinions expressed herein do not necessarily reflect those of the European Commission. Support from CEA and from the French Fédération de Recherche sur la Fusion Magnétique is acknowledged. This work was granted access to the HPC resources of CALMIP supercomputing center under the allocation 2013-P1125. The authors would like to thank A Simonin for his continued support.

References

[1] Faircloth D 2013 Ion sources for high-power hadron accelerators *Proc. CAS-CERN Accelerator School: High Power Hadron Machines* ed R Bailey *(Bilbao, Spain)*
[2] Shishlo A, Galambos J, Aleksandrov A, Lebedev V and Plum M 2012 *Phys. Rev. Lett.* **108** 114801
[3] Hemsworth R and Inoue T 2005 *IEEE Trans. Plasma Sci.* **33** 1799
[4] Fubiani G, Hemsworth R S, de Esch H P L and Svensson L 2009 *Phys. Rev. ST Accel. Beams* **12** 050102
[5] Speth E *et al* 2006 *Nucl. Fusion* **46** S220
[6] Ikeda K, Nakano H, Tsumori K, Kisaki M, Nagaoka K, Osakabe M, Takeiri Y and Kaneko O 2013 *New J. Phys.* **15** 103026
[7] Hemsworth R *et al* 2009 *Nucl. Fusion* **49** 045006
[8] McCracken G and Stott P 2012 *Fusion: The Energy of the Universe* (New York: Academic)
[9] Jacquinot J *et al* 2009 *Proc. 25th Symposium on Fusion Technology (SOFT-25); Fusion Eng. Des.* **84** 125
[10] Fantz U *et al* 2007 *Plasma Phys. Control. Fusion* **49** B563
[11] McNeely P, Dudin S V, Christ-Koch S, Fantz U and the NNBI Team 2009 *Plasma Sources Sci. Technol.* **18** 014011
[12] Wimmer C and Fantz U 2015 *AIP Conf. Proc.* **1655** 040004
[13] Fantz U *et al* 2008 *Rev. Sci. Instrum.* **79** 02A511
[14] Hagelaar G J M, Fubiani G and Boeuf J-P 2011 *Plasma Sources Sci. Technol.* **20** 015001
[15] Boeuf J P, Hagelaar G J M, Sarrailh P, Fubiani G and Kohen N 2011 *Plasma Sources Science and Technology* **20** 015002
[16] Birdsall C K and Langdon A B 1998 *Plasma Physics Via Computer Simulation* (Bristol: IOP Publishing)
[17] Hockney R W and Eastwood J W 1981 *Computer Simulation Using Particles* (New York: McGraw-Hill)
[18] http://openmp.org
[19] Bowers K 2001 *J. Comput. Phys.* **173** 393
[20] Briggs W L, Henson V E and McCormick S F 2000 *A Multigrid Tutorial* (Philadelphia: SIAM)
[21] Fubiani G, Hagelaar G J M, Boeuf J P and Kolev S 2012 *Phys. Plasmas* **19** 043506
[22] Fubiani G and Boeuf J P 2013 *Phys. Plasmas* **20** 113511
[23] Fubiani G and Boeuf J P 2014 *Phys. Plasmas* **21** 073512
[24] Fubiani G and Boeuf J P 2015 *Plasma Sources Sci. Technol.* **24** 055001
[25] Miyamoto K, Okuda S and Hatayama A 2012 *Appl. Phys. Lett.* **100** 233507
[26] Miyamoto K, Okuda S, Hatayama A, Hanada M and Kojima A 2013 *Appl. Phys. Lett.* **102** 023512
[27] Lieberman M A and Lichtenberg A J 2005 *Principles of Plasma Discharges and Materials Processing* (New York: Wiley Interscience)
[28] Nanbu K 2000 *IEEE Trans. Plasma Sci.* **28** 971
[29] Nanbu K 1980 *J. Phys. Soc. Japan* **49** 2042
[30] Bird G 1998 *Molecular Gas Dynamics and the Direct Simulation of Gas Flows* (*Oxford Engineering Science Series*) (Oxford: Clarendon)
[31] Kolev S, Hagelaar G J M and Boeuf J P 2009 *Phys. Plasmas* **16** 042318
[32] Janev R K, Reiter D and Samm U 2003 Collision processes in low-temperature hydrogen plasmas *Technical Report* 4105 FZ-Juelich
[33] Ehrhardt H, Langhans L, Linder F and Taylor H S 1968 *Phys. Rev.* **173** 222

[34] Garvey R H, Porter H S and Green A E S 1977 *J. Appl. Phys.* **48** 4353
[35] Yoon J-S, Song M-Y, Han J-M, Hwang S H, Chang W-S, Lee B and Itikawa Y 2008 *J. Phys. Chem. Ref. Data* **37** 913
[36] England J P, Elford M T and Crompton R W 1988 *Aust. J. Phys.* **41** 573
[37] Gibson D K 1970 *Aust. J. Phys.* **23** 683
[38] Heaps M G and Green A E S 1975 *J. Appl. Phys.* **46** 4718
[39] Gaboriau F and Boeuf J P 2014 *Plasma Sources Sci. Technol.* **23** 065032
[40] Bandyopadhyay M and Wilhelm R 2004 *Rev. Sci. Instrum.* **75** 1720
[41] Krstić P S 2002 *Phys. Rev.* A **66** 042717
[42] Krstić P S 2005 *Nucl. Instrum. Methods Phys. Res.* B **241** 58
[43] Phelps A V 1990 *J. Phys. Chem. Ref. Data* **19** 653
[44] Eirene database (http://eirene.de/html/surface data.html)
[45] Krischok S, Müller H and Kempter V 1999 *Nucl. Instrum. Methods Phys. Res.* B **157** 198
[46] Seidl M, Cui H L, Isenberg J D, Kwon H J, Lee B S and Melnychuk S T 1996 *J. Appl. Phys.* **79** 2896
[47] McNeely P, Wünderlich D and the NNBI Team 2011 *Plasma Sources Sci. Technol.* **20** 045005
[48] Wünderlich D, Gutser R and Fantz U 2009 *Plasma Sources Sci. Technol.* **18** 045031
[49] McAdams R, Holmes A J T, King D B and Surrey E 2011 *Plasma Sources Sci. Technol.* **20** 035023
[50] Cartry G, Schiesko L, Hopf C, Ahmad A, Carrre M, Layet J M, Kumar P and Engeln R 2012 *Phys. Plasmas* **19** 063503
[51] Eckstein W and Biersack J 1985 *Appl. Phys.* A **38** 123
[52] Ando A *et al* 1992 *AIP Conf. Proc.* **287** 339
[53] Ciric D 2006 private communication
[54] Boeuf J P, Claustre J, Chaudhury B and Fubiani G 2012 *Phys. Plasmas* **19** 113510
[55] Boeuf J P, Chaudhury B and Garrigues L 2012 *Phys. Plasmas* **19** 113509
[56] Hagelaar G J M and Oudini N 2011 *Plasma Phys. Control. Fusion* **53** 124032
[57] Ecker G and Kanne H 1964 *Phys. Fluids* **7** 1834
[58] Kunkel W B 1981 *Am. J. Phys.* **49** 733
[59] Gaboriau F, Baude R and Hagelaar G J M 2014 *Appl. Phys. Lett.* **104** 214107
[60] Boeuf J P, Fubiani G and Garrigues L 2016 *Plasma Sources Sci. Technol.* **25** 045010
[61] Leung K N and Bacal M 1984 *Rev. Sci. Instrum.* **55** 338
[62] Schiesko L, McNeely P, Franzen P, Fantz U and the NNBI Team 2012 *Plasma Phys. Control. Fusion* **54** 105002
[63] Schiesko L 2014 private communication
[64] Mochalskyy S, Lifschitz A F and Minea T 2012 *J. Appl. Phys.* **111** 113303
[65] Mochalskyy S, Wünderlich D, Ruf B, Fantz U, Franzen P and Minea T 2014 *Plasma Phys. Control. Fusion* **56** 105001
[66] Taccogna F, Minelli P, Longo S, Capitelli M and Schneider R 2010 *Phys. Plasmas* **17** 063502
[67] Belchenko Y I, Oka Y, Kaneko O, Takeiri Y, Tsumori K, Osakabe M, Ikeda K, Asano E and Kawamoto T 2004 *Rev. Sci. Instrum.* **75** 1726
[68] Kashiwagi M *et al* 2014 *Rev. Sci. Instrum.* **85** 02B320
[69] Garrigues L, Fubiani G and Boeuf J P 2017 *Nucl. Fusion* **57** 014003
[70] Simonin A *et al* 2016 *New J. Phys.* **18** 125005
[71] Itikawa Y 1974 *At. Data Nucl. Data Tables* **14** 1
[72] Janev R K 1995 *Atomic and Molecular Processes in Fusion Edge Plasmas* (Berlin: Springer)
[73] Williams J F 1975a *J. Phys. B: At. Mol. Phys.* **8** 1683
[74] Williams J F 1975b *J. Phys. B: At. Mol. Phys.* **8** 2191
[75] Bray I, Konovalov D A and McCarthy I E 1991 *Phys. Rev.* A **44** 5586
[76] Buckman S J and Phelps A V 1985 *J. Chem. Phys.* **82** 4999
[77] Janev R K 1987 *Elementary Processes in Hydrogen-Helium Plasmas* (Berlin: Springer)
[78] Phelps A V 2009 *Phys. Rev.* E **79** 066401
[79] Krstić P S and Schultz D R 2003 *J. Phys. B: At. Mol. Opt. Phys.* **36** 385
[80] Krstic P S and Schultz D R 1998 *At. Plasma-Mater. Interact. Data Fusion* **8** 1
[81] Barnett C F 1990 Collisions of h, h2, he, and li atoms and ions with atoms and molecules *Technical Report* ORNL-6086 Oak Ridge National Laboratory
[82] Tabata T and Shirai T 2000 *At. Data Nucl. Data Tables* **76** 1